



# WE-NEED

WatEr NEEDs, availability, quality and sustainability



<b>Deliverable Number:</b>	D2.2
<b>Work package number:</b>	WP2
<b>Deliverable title</b>	REPORT ON GROUNDWATER FLOW AND TRANSPORT ON THE TWO FIELD SITES
<b>Type</b>	Report
<b>Dissemination Level</b>	Public
<b>Lead participant</b>	UPC
<b>Contributing scientists and other personnel</b>	Daniel Fernàndez-Garcia, Guillem Sole-Mari, Emanuela Bianchi Janetti, Martina Siena, Ceriotti Giulia, Dell'Oca Aronne, Alberto Guadagnini, Giovanni M Porta, Monica Riva
<b>Scheduled delivery date</b>	20/08/2018
<b>Actual / forecast delivery date</b>	20/11/2018

## Deliverable summary

This document describes the numerical flow and transport models developed for the two field sites analyzed in the project: Cremona and Bologna Aquifer systems, located in the Po Plain, Northern Italy. We implement a backward particle tracking model to characterize the water extracted by the pumping wells in terms of land use signature and residence time. The stochastic solute transport results are based on the velocity fields resulting from the multiple stochastic realizations described in Deliverable D1.4b. The transport results are then discussed globally and individually for the main extraction wells. Finally, we describe the approach that we will follow for the probabilistic risk assessment task.



## D2.2

# Report on groundwater flow and transport on the two field sites

### Contents

1. Cremona site .....	3
1.1 Conceptual and Numerical model .....	3
1.2 Results and discussion .....	3
1.3 Ongoing and future planned activities .....	5
2. Bologna site .....	6
2.1 Conceptual and Numerical model .....	6
2.2 Results and discussion .....	10
2.3 Ongoing and future planned activities .....	14
References .....	16
Appendix: Results overview of Bologna solute transport simulations .....	16



## 1. Cremona site

The study area is part of the high-medium Alluvial Po Plain. It lies between the city of Bergamo (Northern Italy) and the confluence of the Adda and Serio rivers (see Figure 2.1 of Deliverable 1.4a). A key feature of the study area is the occurrence of high-quality water springs, which are the main supply to agriculture and a key environmental driver.

### 1.1 Conceptual and Numerical model

In Deliverable 1.4a and 1.4b we developed a conceptual and a numerical model of the study area. In particular, on the bases of lithological data, we reconstructed the three dimensional distribution of facies within the aquifer by means of two geostatistical methods: the Composite medium approach (*CM*) and the Overlapping Continuum Approach (*OC*). Then, we analysed the impact of the uncertainty in (a) the conceptual model (the two variants of *OC* versus *CM*), (b) the boundary conditions and (c) the hydraulic parameters on the groundwater system response, as quantified in terms of steady-state hydraulic heads obtained at a set of 39 target locations, covering the full investigated area. This analysis has been performed by relying on three Global Sensitivity Analysis, GSA, methodologies: (a) a derivative-based approach, which rests on the Morris indices (Morris, 1991), (b) a variance-based approach, grounded on the evaluation of the Sobol' indices (Sobol, 1993, 2001) and (c) a moment-based GSA, which takes into account the influence of uncertain parameters on multiple (statistical) moments of model outputs of interest (Dell'Oca et al., 2017). We then use results of GSA to drive calibration of model parameters including the most influential hydraulic conductivity values of the geomaterials composing the aquifer and natural springs leakage coefficient.

In the present document we provide the analysis of groundwater flow obtained with the calibrated *CM* and *OC* models described in Deliverable 1.4b. *OC* models are termed as *OC\_A* and *OC\_G*, when considering the arithmetic or geometric averaging operator, respectively.

### 1.2 Results and discussion

Parameter estimates and related estimation error standard deviation for the three calibrated models are reported in Tables 2.1 and 2.3 of Deliverable 1.4b. Figures 1.1 shows the distribution of the hydraulic heads within the study area for *CM*, *OC\_A* and *OC\_G* calibrated models. The main flow direction is from North to South. The hydraulic gradient slightly decreases from North to South, with a mean value of approximately 3.7‰. One can note that the distribution of hydraulic head in the calibrated models do not present significant difference among the three considered model approaches. As discussed in Section 2.2 of Deliverable 1.4b, all three calibrated models are accurate in reproducing the behaviour of the main flow feature of the site (e.g., hydraulic heads and mean annual total discharge at the natural springs).

The diverse water balance terms evaluated for all developed models are depicted in Figures 1.2. All incoming terms are indicated with subscript “in” while quantities outflowing



from the aquifer are indicated with subscript “out”. The conceptual model mainly affects the amount of water entering and/or leaving the aquifer through the Western and Eastern boundaries of the domain (which correspond to the flow path of Adda and Serio rivers). All remaining terms are not significantly affected by model conceptualization.

Figure 1.3 shows sample pdfs of logconductivity ( $Y$ ) for  $OC\_A$  and  $OC\_G$  calibrated models. Also shown for comparison are Gaussian distributions having the same mean and variance as the sample pdfs and the sample pdf evaluated for the  $CM$  calibrated models. As we discussed in Section 2.3 of Deliverable 1.4a, we note that the two diverse averaging strategies may significantly affect the spatial distribution of  $Y$ . Considering the calibrated models, the difference between the logconductivity sample pdfs evaluated with the  $OC\_A$  and  $OC\_G$  methodologies is reduced respect to the not calibrated models (see Figure 2.9 of Deliverable 1.4a). This finding is related to the fact that larger values of conductivities are obtained for  $OC\_G$  calibrated model with respect to  $OC\_A$ -based counterparts (see Table 2.3 of Deliverable 1.4b). This notwithstanding, the domain is still (on average) more permeable and less heterogeneous when the arithmetic rather than the geometric mean operator is employed.

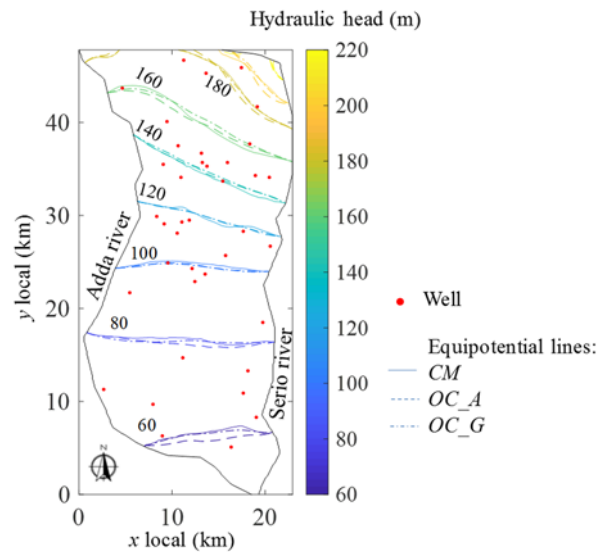


Figure 1.1 Spatial variation of hydraulic heads associated with  $CM$ ,  $OC\_A$ , and  $OC\_G$  calibrated models. Location of monitoring wells is also reported.

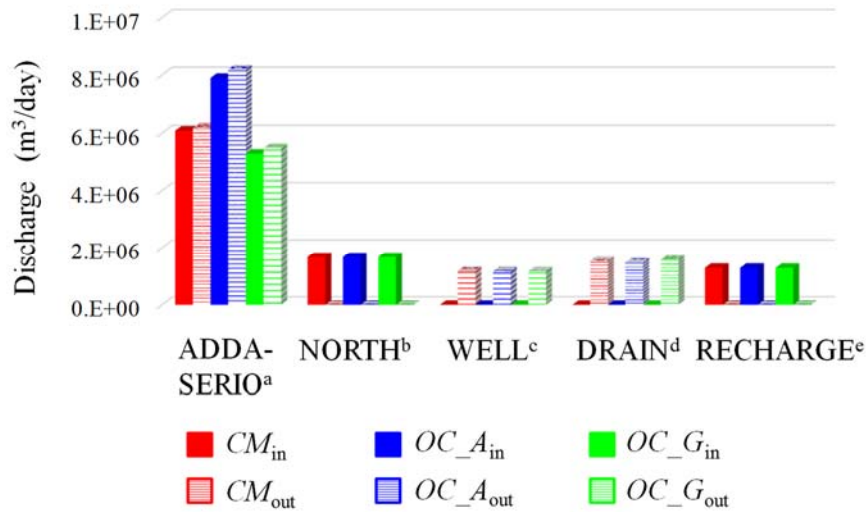


Figure 1.2. Water balance terms evaluated for  $CM$ ,  $OC\_A$ , and  $OC\_G$  calibrated models. Different terms correspond to flow rates due to (a) Eastern and Western domain boundaries, (b) Northern domain boundary, (c) pumping wells, (d) natural springs and (e) recharge from infiltrations.

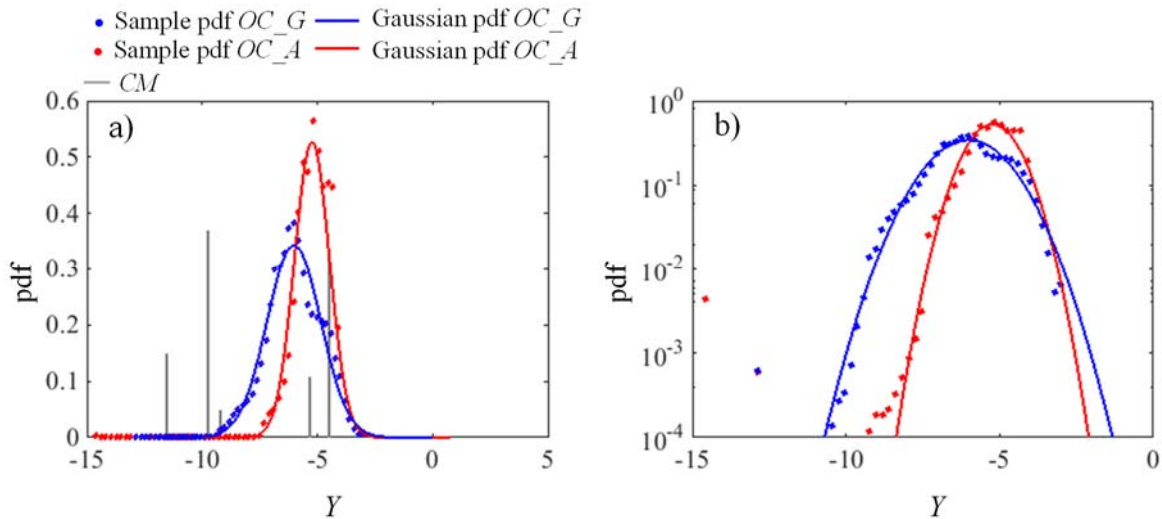


Figure 1.3 Sample pdfs of logconductivity ( $Y$ ) for  $OC\_A$  and  $OC\_G$  on (a) natural and (b) semi logarithmic scales. Also shown for comparison are (i) Gaussian distributions having the same mean and variance as the sample pdfs and (ii) the sample pdf evaluated for the  $CM$  model. Results correspond to the fields associated with calibrated models.

### 1.3 Ongoing and future planned activities

Currently we are working in the context of WP2.3 and WP5.2. We are planning to (i) evaluate probabilistic protection zones for the natural springs located in the study area and (ii) apply the groundwater risk management model to the Cremona site. In particular, we will focus on the evaluation of the effect of pumping rates on the natural springs within the system in order to preserve them from depletion.



## 2. Bologna site

### 2.1 Conceptual and Numerical model

The Bologna aquifer system is located in the lower part of the Po plain (Emilia Romagna region, Northern Italy). The investigated domain extends over  $20 \times 23 \text{ km}^2$  in the horizontal plane and from -450 m to 100 m a.s.l. along the vertical direction. A complete characterization of the site is provided by Deliverables 1.4a and 1.4b. Lithological data available from more than 1300 boreholes allowed to identify 4 main categories within the area: clay, gravel, silt and sand, with volumetric fraction  $p_1 = 0.523$ ,  $p_2 = 0.281$ ,  $p_3 = 0.133$  and  $p_4 = 0.063$  respectively. As detailed in Deliverables 1.4a and 1.4b, we applied two diverse geostatistical reconstruction techniques to describe the architecture of the aquifer system: SISIM, a classic sequential-indicator approach (Deutsch and Journel, 1992) and TPROGS, a transition-probability based method (Carle and Fogg, 1996, 1997). The two techniques have been compared in a Monte Carlo (MC) framework, by relying on two sets of  $n = 100$  realizations conditioned on lithological data. The comparison has been performed in terms of (i) ensemble variograms and transiograms; (ii) degree of facies connectivity; (iii) calibration of facies hydraulic conductivities; (iv) model discrimination criteria and (v) multi-model predictions of hydraulic heads. We observed that, for all geomaterials, the TPROGS set exhibits larger correlation lengths and a higher degree of connectivity with respect to SISIM counterparts. The most relevant difference between the two generation methods in terms of connectivity concerns gravel, which is much more fragmented in SISIM realizations. Since gravel is the most conductive facies in our domain, this also affects the calibration of flow parameters: in SISIM we obtained larger hydraulic conductivity estimates, compensating for the smaller degree of connectivity. The comparison in terms of model discrimination criteria clarifies that the best realization (identified on the basis of model discrimination/identification criteria) within the TPROGS set provides better results according to all criteria with respect to its counterpart in SISIM (see Table 3.1 of Deliverable 1.4b). Finally, multi-model head estimates obtained from all MC realizations of the TPROGS set show a better agreement with the head measurements available at the monitoring wells. These results led us to focus on the set of TPROGS realizations for the following investigations on the Bologna site. In the present document we illustrate the results of groundwater flow and transport simulations performed within the TPROGS set of MC realizations.

We perform steady-state simulations of groundwater flow in each MC realization of the TPROGS set. The numerical model adopted here shares almost all features with the one described in Section 3.2 of Deliverable 1.4b, except for two aspects:

- (i) For each realization, we use the corresponding hydraulic conductivity estimates resulting from model calibration (see Section 3.3 of Deliverable 1.4b);



- (ii) To improve the accuracy of the flow field required by the transport model, we increase the grid resolution in the urban region of Bologna, where the most important well fields are located. As illustrated by Fig. 2.1, the grid size along both horizontal axes decreases progressively from 500 m to 125 m.

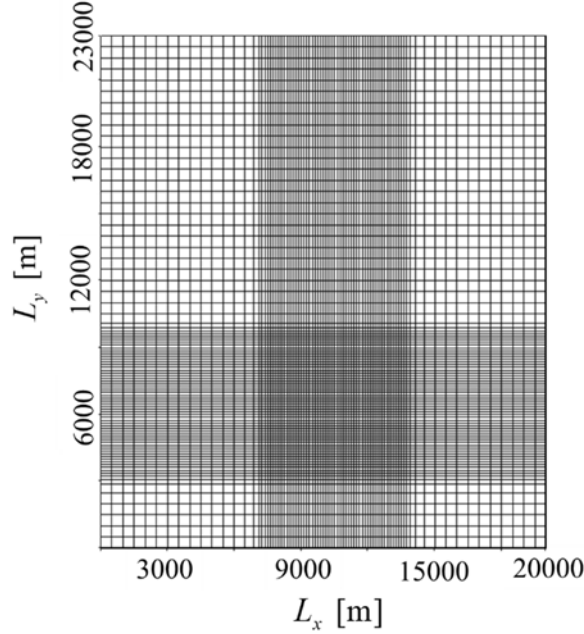


Figure 2.1. Refined grid used for groundwater flow-transport simulations.

We simulate the solute transport via a backward-in-time advection technique, which allows us to detect the origin of the water reaching the extraction wells and as well as the travel time distributions.

Pollock's method in  $d$  dimensions (Pollock, 1988; 1994) defines the particle velocity as the  $d$ -linear interpolation of the interface velocities at any point  $\mathbf{X} \in \Omega$ , where  $\Omega$  is a flow cell:

$$\mathbf{V} = \mathbf{v}(\mathbf{X} \in \Omega) = (\mathbf{1} - \hat{\mathbf{X}}) \odot \mathbf{v}_{\Omega}^{-} + \hat{\mathbf{X}} \odot \mathbf{v}_{\Omega}^{+} \quad (2.1)$$

Where  $\mathbf{X}$  is the particle position,  $\mathbf{V}$  is the particle velocity,  $\hat{\mathbf{X}} = (\mathbf{X} - \mathbf{x}_{\Omega}^{-}) \oslash (\mathbf{x}_{\Omega}^{+} - \mathbf{x}_{\Omega}^{-})$ ,  $\mathbf{1}$  is a  $d \times 1$  vector of ones, operators " $\odot$ " and " $\oslash$ " stand for the elementwise or Hadamard product and division, respectively,  $\mathbf{x}_{\Omega}^{-}$  and  $\mathbf{x}_{\Omega}^{+}$  are 3-element vectors containing the lower and upper cell interface location for each direction, and  $\mathbf{v}_{\Omega}^{-}$  and  $\mathbf{v}_{\Omega}^{+}$  are also 3-element vectors containing the corresponding cross-interface flow velocities (obtained in the numerical solution of the flow problem). By definition:

$$\frac{\partial \hat{\mathbf{X}}}{\partial t} = \frac{\partial \hat{\mathbf{X}}}{\partial \mathbf{X}^T} \frac{\partial \mathbf{X}}{\partial t} = \mathbf{V}(\mathbf{X}) \oslash \Delta \mathbf{x}_{\Omega} = (\mathbf{v}_{\Omega}^{-} + \Delta \mathbf{v}_{\Omega} \hat{\mathbf{X}}) \oslash \Delta \mathbf{x}_{\Omega} \quad (2.2)$$



Where  $\Delta \mathbf{x}_\Omega = \mathbf{x}_\Omega^+ - \mathbf{x}_\Omega^-$  and  $\Delta \mathbf{v}_\Omega = \mathbf{v}_\Omega^+ - \mathbf{v}_\Omega^-$ . Integrating expression (2.2), given the initial velocity  $\mathbf{V}(t)$ , we can determine the possible lapses of time in which the particle would reach either end of the cell:

$$\Delta t^+ = (\Delta \mathbf{x}_\Omega \oslash \Delta \mathbf{v}_\Omega) \ln(\mathbf{v}_\Omega^+ \oslash \mathbf{V}(t)), \quad \Delta t^- = (\Delta \mathbf{x}_\Omega \oslash \Delta \mathbf{v}_\Omega) \ln(\mathbf{v}_\Omega^- \oslash \mathbf{V}(t)) \quad (2.3)$$

In three dimensions, this gives six possible solutions, among which we choose the actual  $\Delta t$  as the minimum positive entry in  $\Delta t^+$  or  $\Delta t^-$ ; then the position of the particle at the end of the step is:

$$\mathbf{X}(t + \Delta t) = (\Delta \mathbf{x}_\Omega \oslash \Delta \mathbf{v}_\Omega) \odot (\mathbf{V}(t) \odot \exp(\Delta t \Delta \mathbf{v}_\Omega \oslash \Delta \mathbf{x}_\Omega) - \mathbf{v}_\Omega^-) \quad (2.4)$$

In order to perform backward simulations, the velocity field is reversed, i.e.

$$\mathbf{v} = -\mathbf{v}^* \quad (2.5)$$

Where  $\mathbf{v}^*$  is the actual (forward-in-time) velocity field. The combined reiterated computation of expressions (2.3) and (2.4) allows to track the path of a particle of fluid in time.

Land use data was obtained from the 2012 Corine Land Cover inventory (Bosard et al., 2000), which contains information of land cover over 27 countries in Europe on a 100 m resolution. The geographical data was projected on the model domain with a  $500 \times 500 \text{ m}^2$  grid, obtaining the distribution of land cover on each cell of the grid. Figure 2.2 shows the dominant land cover on each cell. Based on this, we assigned a signature to the recharge water based on the land use distribution at its entry plane.

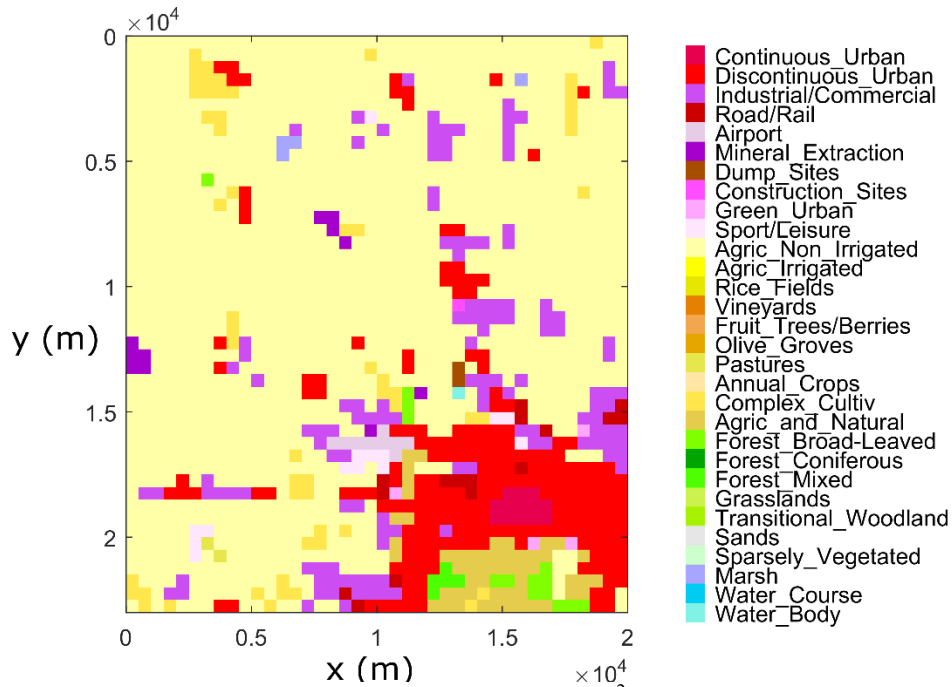


Figure 2.2. Dominant land cover on a  $500 \times 500 \text{ m}^2$  grid of the model domain, interpolated from Corine Land Cover data.





We implement the previously described backward Pollock's methodology to track particles backwards in time from the wells to either the top of the aquifer or the domain limits. The particle injection is done uniformly on the interfaces that delimitate the cells where the well screens are located (see Figure 2.3). To each particle  $i$  is assigned a mass  $m_i$  proportional to the water velocity towards the well at its injection point. If water is flowing in the opposite direction, the assigned mass is zero. By doing this, under the assumption of a well-mixed condition inside the well cells, the particle mass distribution is proportional to the contribution of their injection position to the water extracted by the well. The density of particles injected per unit surface was  $0.4 \text{ m}^{-2}$ .

For each injected particle, expressions (2.3) and (2.4) are computed until the source (the top of the aquifer or the domain limits) is reached, and the particle is assigned the land-use signature distribution  $P_i(\mathcal{L}_j)$  corresponding to its source,  $\mathcal{L}_j$  being the  $j$ th land use definition. The total time spent in the aquifer,  $T_i$ , is also recorded.

The ensemble distributions are then obtained from the information on all particles at a given well. The discrete land use portions  $P(\mathcal{L}_j)$  are obtained as

$$P(\mathcal{L}_j) = \frac{\sum_{i=1}^N m_i P_i(\mathcal{L}_j)}{\sum_{i=1}^N m_i I_i} \quad (2.6)$$

$N$  being the number of particles (computed as the particle density multiplied by the well-screen area) and  $I_i$  being an indicator function defined as 1 if the particle  $i$  reached the top of the aquifer and 0 otherwise. The distribution of arrival times is a continuous function that can be estimated from the finite particle arrival times. In order to present the results (see the Appendix), a histogram of the log-residence times is computed, i.e.

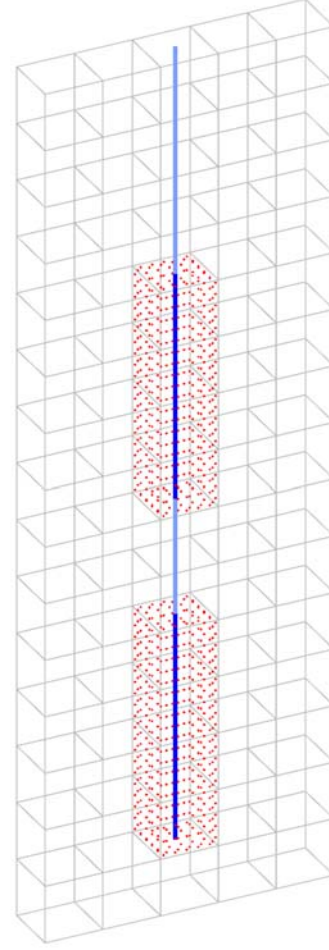


Figure 2.3. Scheme of particle injection at a well for backward particle tracking. In gray, the numerical grid of the velocity field; In dark and light blue, the screened and the impermeable parts of the well, respectively; In red, the injected particles.

$$P(\log_{10} T_k; g) = \frac{\sum_{i=1}^N m_i \mathcal{H} \left( \log_{10} T_i - \log_{10} T_k + \frac{g}{2} \right) \mathcal{H} \left( -\log_{10} T_i + \log_{10} T_k + \frac{g}{2} \right) I_i}{\sum_{i=1}^N m_i I_i} \quad (2.7)$$

Where  $T_k$  belongs to a discrete set of values such that  $\log_{10} T_{k+1} = \log_{10} T_k + g$ , and  $\mathcal{H}$  is the Heaviside step function. We set  $g = 0.1$ .

## 2.2 Results and discussion

Figures 2.4a and 2.5a depict head contour lines respectively along a horizontal and a vertical cross section obtained for a selected TPROGS realization where KIC is minimum. Pumping wells are represented as red symbols with size proportional to the associated withdrawal rate in Fig. 2.4a. In Fig. 2.5a, well screens are reported as black thick lines. The distribution of hydraulic heads is characterized by an evident cone of drawdown centered on the main well fields in the Bologna urban area. Comparison among Fig. 2.4b and 2.5b indicates that the distribution of head is substantially affected by the spatial arrangement of geomaterials: regions of large hydraulic heads are associated with clay, which offers a large resistance to flow. Analogous conclusions can be drawn from the observation of head distribution in all realizations.

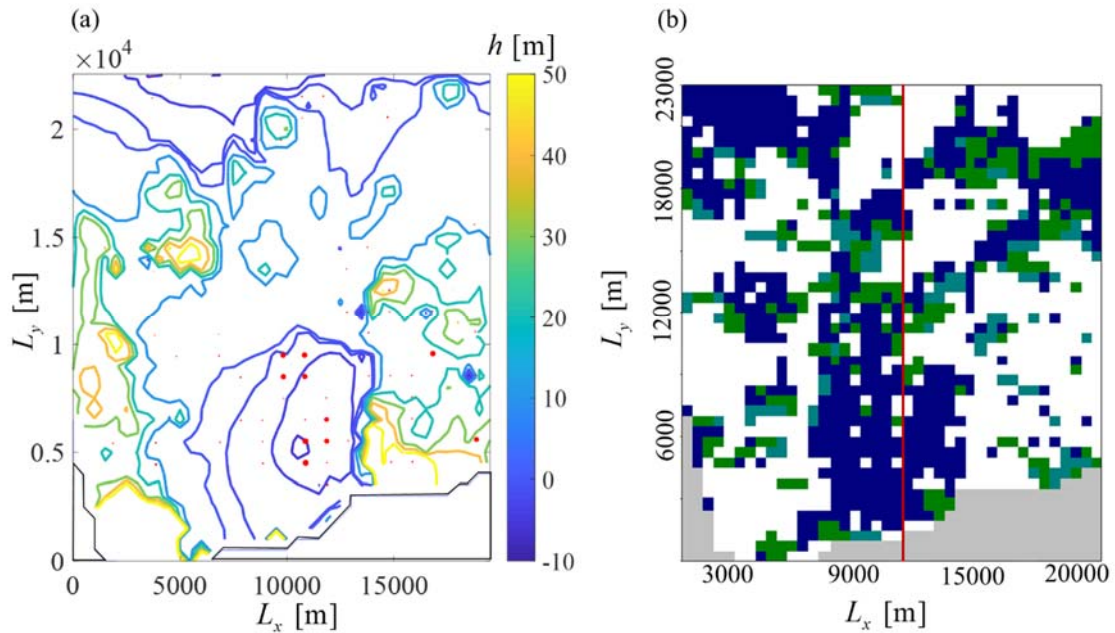


Figure 2.4. (a) Distribution of hydraulic heads and (b) corresponding facies distribution along a horizontal cross section of one MC realization. In (a), pumping wells are represented as red dots, with size proportional to the withdrawal rate. In (b), the red line indicates the position of the vertical cross section depicted in Fig. 2.5.

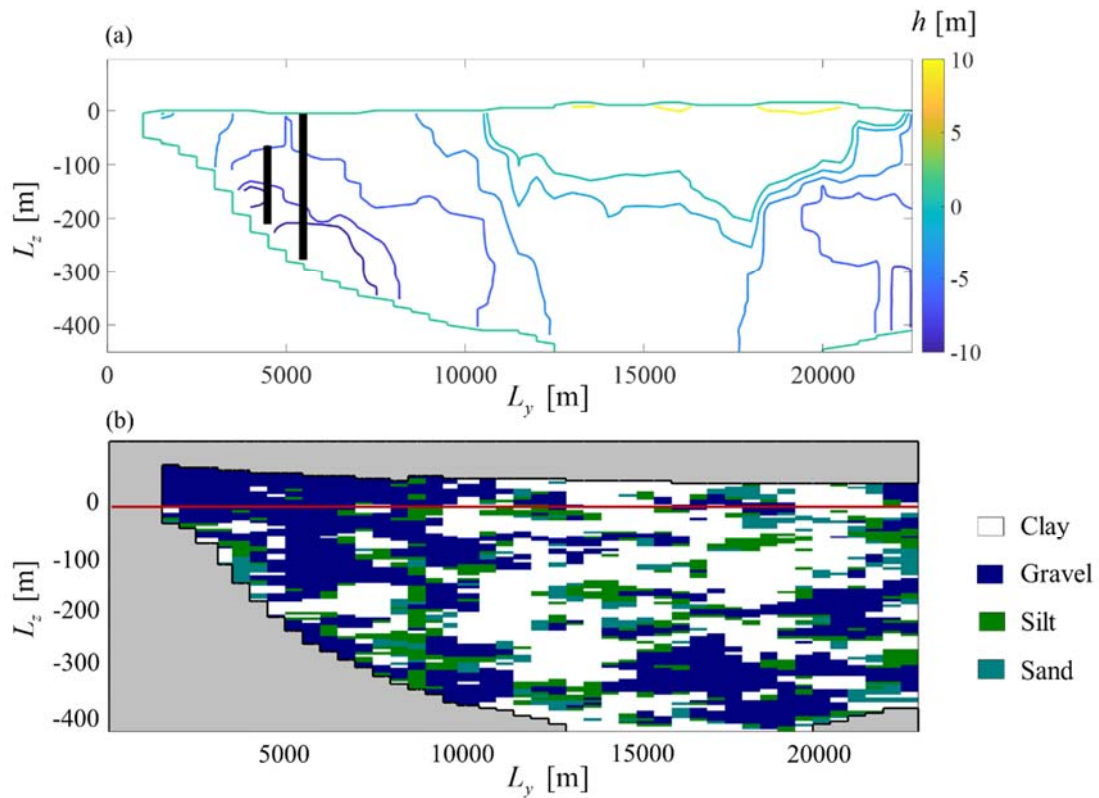


Figure 2.5. (a) Distribution of hydraulic heads and (b) facies along a vertical cross section of one MC realization. In (a), well screens are represented as black vertical thick lines. In (b), the red line indicates the position of the horizontal cross section depicted in Fig. 2.4.

Figures 2.6 illustrate the magnitude of the diverse contributions to groundwater balance: both inflow and outflow rates are associated with the lateral prescribed-head boundaries; wells discharge and surface recharge rates contribute respectively as outflow and inflow terms.

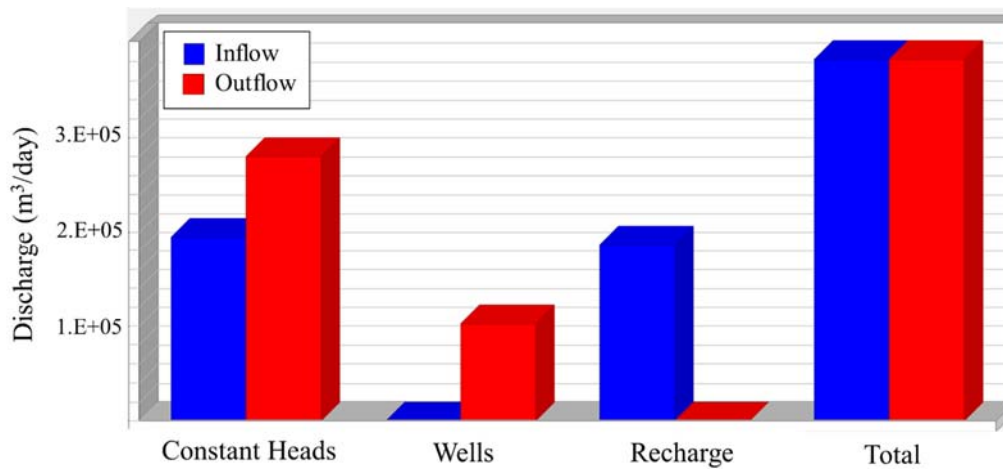


Figure 2.6. Contributions to groundwater balance in the numerical model. The diverse terms correspond to (i) constant-head boundaries, (ii) pumping wells and (iii) recharge from infiltrations.



In the following we overview and discuss the transport results at the Bologna site for 10 selected wells, corresponding to the 10 highest yearly extraction flow rates. These wells are labelled as Well 1-10 in this report for simplicity. Table 2.1 shows their position in the numerical model, together with the groundwater use and the well-field name associated with the actual wells that they represent. The plots showing the discussed wells' locations, capture zones, travel time distributions and land use signature distributions for realizations 0-8 can be found in the Appendix. This selection of the data has been made for the sake of conciseness in this report. Model outputs corresponding to all wells and realizations are available. These outputs will be used in the risk assessment WP.

WELL	X (m)	Y(m)	GROUNDWATER USE	WELL FIELD
1	16750.0	5937.5	Industrial	-
2	9812.5	6062.5	Public supply	San Vitale
3	10812.5	7062.5	Public supply	San Vitale
4	11937.5	8937.5	Public supply	Tiro a Segno
5	10812.5	6062.5	Public supply	San Vitale
6	9812.5	7062.5	Public supply	San Vitale
7	18750.0	9999.0	Public supply/Industrial	Fossolo
8	10937.5	10311.5	Public supply	Borgo Panigale
9	11937.5	9999.0	Public supply	Tiro a Segno
10	10937.5	14250.0	Public supply	Borgo Panigale

Table 2.1. Position, groundwater use and well-field name associated to each one of the 10 selected wells considered in this report.

In all realizations and for all wells, the dominant land use signature of the extracted water that comes from the model area is agricultural non-irrigated, as would be expected since most of the aquifer is covered by this type of land. However, the results clearly differ between the diverse wells, both in terms of land use signature and residence times (which can range from less than 1 year to about  $10^4$  years). Results at different wells also display different degrees of variability between individual realizations. In most realizations and wells, the main source of water comes from inside the model domain. The stochastic nature of the velocity field results in a wide variety of capture zones typically predicted for the same well, which points out the limitations of classical approaches that simply delimitate well protection areas as a function of the radial distance to the well.

Note from eq. 2.6 that the land use values  $P(L_j)$  are normalized with respect to the total water coming from the domain. Therefore, the value for boundary (BD) may exceed 1, in which case it will exceed the plot limits. Similarly, values of  $P(\log_{10} T)$  exceeding 0.2 are plotted as 0.2.

Well 1 (Figure A.1): The results at this well are characterised by very long residence times, such that in all realizations the residence time is larger than 100 years. Some realizations show an important contribution of water from the limits of the model. Many realizations show a contribution of industrial, discontinuous urban and complex cultivation of  $\leq 10\%$ .



Well 2 (Figure A.2): The residence times of the water extracted from this well show a strong variability among realizations, with minimums ranging from less than 10 years to almost 100 years. Other contributions than agricultural are very rarely predicted, and some realizations show a very important contribution from the boundary.

Well 3 (Figure A.3): Residence times of the water extracted at this well are moderately low, with consistent predictions of the minimum at about 10 years, and in some cases at about 5 years. Some realizations show a contribution from a mineral extraction site. Most realizations also show some small contributions of industrial and suburban areas, and in some most of the extracted water comes from outside the model domain.

Well 4 (Figure A.4): Residence times at this well consistently have minima in the order of 10 years. Land use results for this well show particularly high contributions of industrial and discontinuous urban areas, adding up to almost 40% of the total extracted water in some cases. Several realizations also show a small contribution of dump sites, construction sites and mining areas.

Well 5 (Figure A.5): Results for the residence time of water extracted at this well are highly variable between realizations, with minima ranging from about 10 to 100 years. Areas with complex cultivation patterns contribute to the extracted water in most realizations, and so do industrial and suburban areas. A small contribution from mining areas and forests also occurs in some cases.

Well 6 (Figure A.6): Several realizations for this well show minimum residence times in the order of the year. However, the portion of water that these low residence times represent is always very small. In most realizations there is a contribution from the boundary, very high in some of them. Small contributions of industrial, suburban, airport and marsh are also present, as well as a moderate contribution of complex cultivation pattern areas. In one realization, the results show a contribution of a mineral extraction site of about 10% of the water coming from the model domain.

Well 7 (Figure A.7): Results for this well consistently show very low residence times (1 year or less in some cases) and small capture zones. Most of the extracted water comes from outside the model domain, the rest coming mainly from agricultural non-irrigated, but also complex cultivation pattern areas and in some cases discontinuous urban areas.

Well 8 (Figure A.8): This well is characterized by moderate to low residence times, with a relatively small variability among realizations. Many different land use signatures apart from agricultural non-irrigated contribute to the extracted water, including discontinuous urban, industrial, mining, complex cultivation, forest, and marsh. The contribution of the boundary is small in most realizations.

Well 9 (Figure A.9): Results show moderately low minimum residence times (around 10 years) for the water extracted at this well. Most realizations show a particularly high contribution of





industrial and suburban areas (up to 20%), as well as small contributions from mining and dump sites.

Well 10 (Figure A.10): Typical residence times for water extracted at this well are even lower than at Well 9, with predicted minima often below 5 years. Some small contribution of sports and leisure areas is observed in most realizations, as well as some contributions of industrial, discontinuous urban and complex cultivation pattern areas.

### 2.3 Ongoing and future planned activities

We plan to perform a risk assessment based on the results of the transport model. By selecting the contaminants of interest, and setting an initial concentration in the aquifer recharge water, the expected concentration in the extracted water can be derived. Without considering degradation or sorption, if  $\mathbf{c}$  is a vector containing all the considered species' concentrations at the well in one realization, and  $\mathbf{c}_0^j$  is the input concentrations considered for land use  $j$ , one obtains

$$\mathbf{c} = \sum P(\mathcal{L}_j) \mathbf{c}_0^j \quad (2.8)$$

If degradation is considered, the residence time distribution specific to each land use signature can be used to correct expression (8). From the concentration values obtained in all realizations, the individual risk to human health and to the environment associated to each of the species can be evaluated.

Additionally, we are interested in evaluating the effect on the risk of the interaction between different chemical species. To do this, we will use a risk model that considers synergistic and antagonism effects associated with a chemical mixture (Jonker et al., 2005). Routine risk analysis consider that the actual effect of the mixture is adequately described by risk metric addition. Let us consider  $R_i$  to be the risk posed by an individual contaminant  $i$  of a chemical mixture composed of  $n$  contaminants, the additive risk model states that the total risk  $R_T$  posed by the exposure to a chemical mixture can be satisfactorily determined by the sum of individual risks,

$$R_T \approx RA = \sum_{i=1}^n R_i \quad (2.9)$$

However, current data show that more complex response patterns, such as dose-dependent synergism/antagonism, do occur in real life. Based on Jonker et al. (2005) model, the above additive risk model can be generalized as follows

$$R_T = RA \times \exp(G) \quad (2.10)$$



Where the function  $G$  expresses the degree of deviations from risk addition. When  $G=0$ , the total risk reduces to the additive model. The deviation function  $G$  depends on the relative contribution of each chemical compound to risk, which can be measured as  $z_i = R_i/RA$ . The deviation function will be written as a function of these relative contributions to risk rather than chemical concentrations.

$$G = G(z_1, \dots, z_n) \quad (2.11)$$

Synergism or antagonism can be described by employing the following deviation function

$$G(z_1, \dots, z_n) = a \prod_{i=1}^n z_i \quad (2.12)$$

This deviation function describes antagonism when parameter  $a$  is positive and synergism when  $a$  is negative. The risk measure can be chosen arbitrarily depend on the effect to human health or the ecosystem. For quantifying the risk due to chronic exposure on human health, one typically expresses that

$$R_i = \beta_i q_i C_i \quad (2.13)$$

where  $C_i$  is the contaminant concentration,  $q_i$  is the is the metabolized cancer potency factor related to the carcinogenic contaminant  $i$ , and

$$\beta_i = \left[ \frac{IR}{BW} \right] \times \frac{ED \times EF}{AT} \quad (2.14)$$

where  $IR$  is the ingestion rate of water (L/d),  $BW$  is the body weight (kg),  $AT$  is the expected lifetime (day),  $ED$  is the exposure duration (year), and  $EF$  is the daily exposure frequency (d/yr). For quantifying the potential for developing non-cancer health effects as a result of exposure, the risk measure can be expressed as

$$R_i = \frac{C_i}{RfC_i} \quad (2.15)$$

Where  $RfC_i$  is a reference concentration of a chemical the exposure of which over specific exposure duration poses no appreciable risk of adverse health effects, even to sensitive populations.



## References

- Bosard, M., Feranec, J., Otahel, J. 2000. *CORINE Land Cover Technical Guide — Addendum 2000*. European Environmental Agency Technical Report No. 40, Copenhagen, Denmark.
- Carle, S.F., Fogg, G.E. 1996. Transition probability-based indicator geostatistics. *Math. Geol.* 28, 4, 453-477.
- Carle, S. F., Fogg, G.E. 1997. Modelling spatial variability with one and multidimensional continuous-lag Markov chains. *Math. Geol.* 29, 7, 891-918.
- Dell'Oca, A., Riva, M., Guadagnini, A. 2017. Moment-based metrics for global sensitivity analysis of hydrological systems. *Hydrol. Earth Syst. Sci.* 21, 6219-6234. <https://doi.org/10.5194/hess-21-6219-2017>.
- Deutsch C.V., Journel A.G. 1992. *GSLIB, Geostatistical software library and user's guide*. New York, Oxford, Oxford university press.
- Jonker, M.J.I., Svendsen, C., Bedaux, J.J., Bongers, M., Kammenga, J.E. 2005. Significance testing of synergistic/antagonistic, dose level-dependent, or dose ratio-dependent effects in mixture dose-response analysis. *Environ Toxicol Chem.*, 10 .2701-13.
- Morris, M.D., 1991. Factorial sampling plans for preliminary computational experiments. *Technometrics* 33, 161–174.
- Pollock, D.W. (1988). Semianalytical computation of pathlines for finite-difference models. *Ground Water* 26, 743.
- Pollock, D.W. (1994). User's guide for MODPATH/MODPATHPLOT, Version 3: A particle tracking post-processing package for MODFLOW. The U.S. Geological Survey finite-difference groundwater flow model. U.S. Geological Survey Open-File Report 94-464, Reston,VA: U.S. Geological Survey
- Sobol, I.M., 1993. Sensitivity estimates for nonlinear mathematical models. *Math. Modeling. Comput.* 1, 407–414.
- Sobol, I. M., 2001. Global sensitivity indices for nonlinear mathematical models and their Monte Carlo estimates. *Math. Comput. Simulat.* 55(1–3), 271–280. doi: 0.1016/S0378-4754(00)00270-6.





## Appendix: Results overview of Bologna solute transport simulations

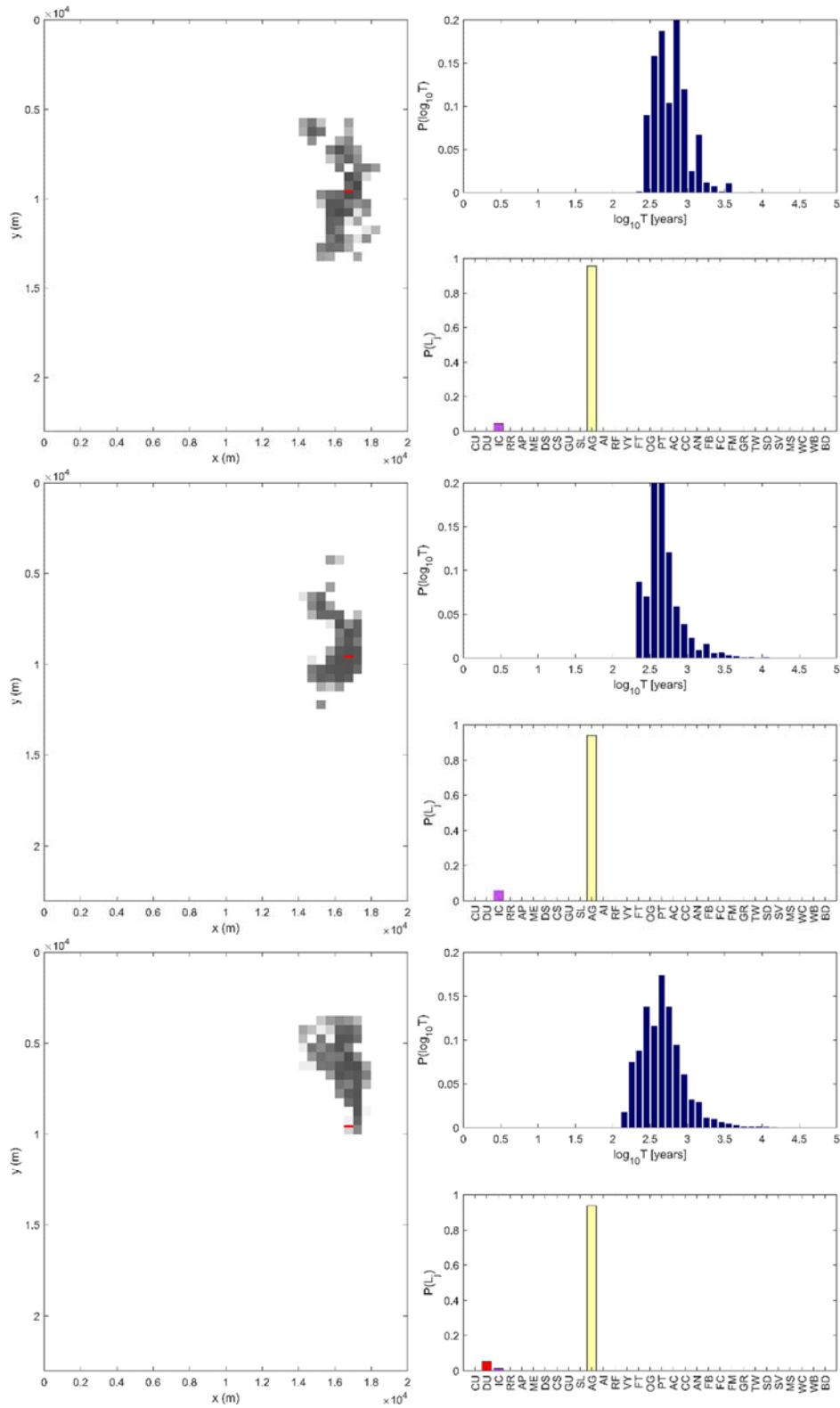


Figure A.1a: Transport results corresponding to Bologna Well 1, realizations 0-2 (top to bottom). In the grayscale map on the left, each cell is colored according to the value of  $\log_{10} F$ , being  $F$  the fraction of the  $N$  particles that are traced back up to the considered cell (white is  $\leq -4$ , black is 0). Pumping Well in red. On the upper-right, histogram of the log-residence time (eq. 2.7). On the bottom-right, land use distribution (eq. 2.6; see Figure 2.2).

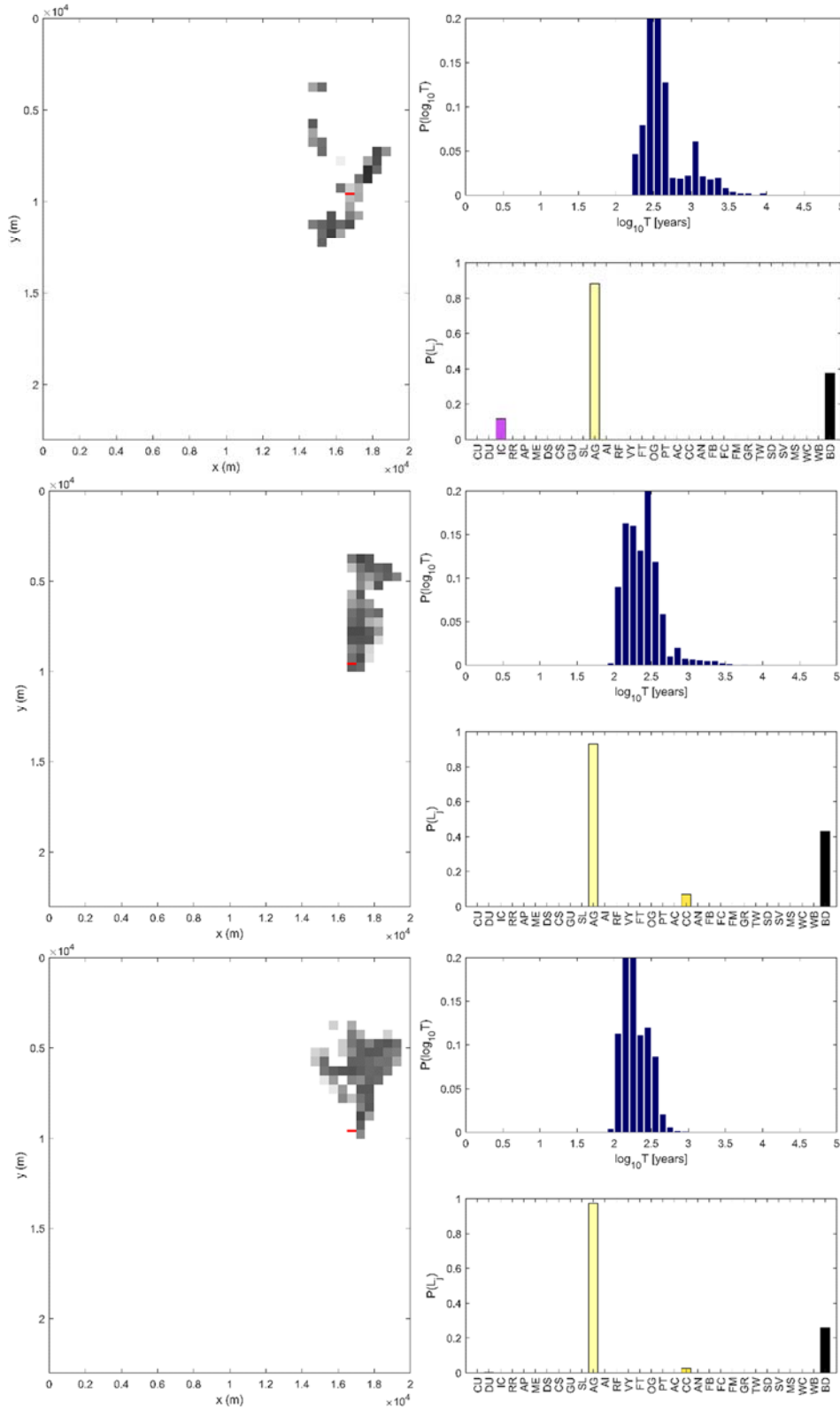


Figure A.1b: Transport results corresponding to Bologna Well 1, realizations 3-5 (top to bottom). In the grayscale map on the left, each cell is colored according to the value of  $\log_{10} F$ , being  $F$  the fraction of the  $N$  particles that are traced back up to the considered cell (white is  $\leq -4$ , black is 0). Pumping Well in red. On the upper-right, histogram of the log-residence time (eq. 2.7). On the bottom-right, land use distribution (eq. 2.6; see Figure 2.2).

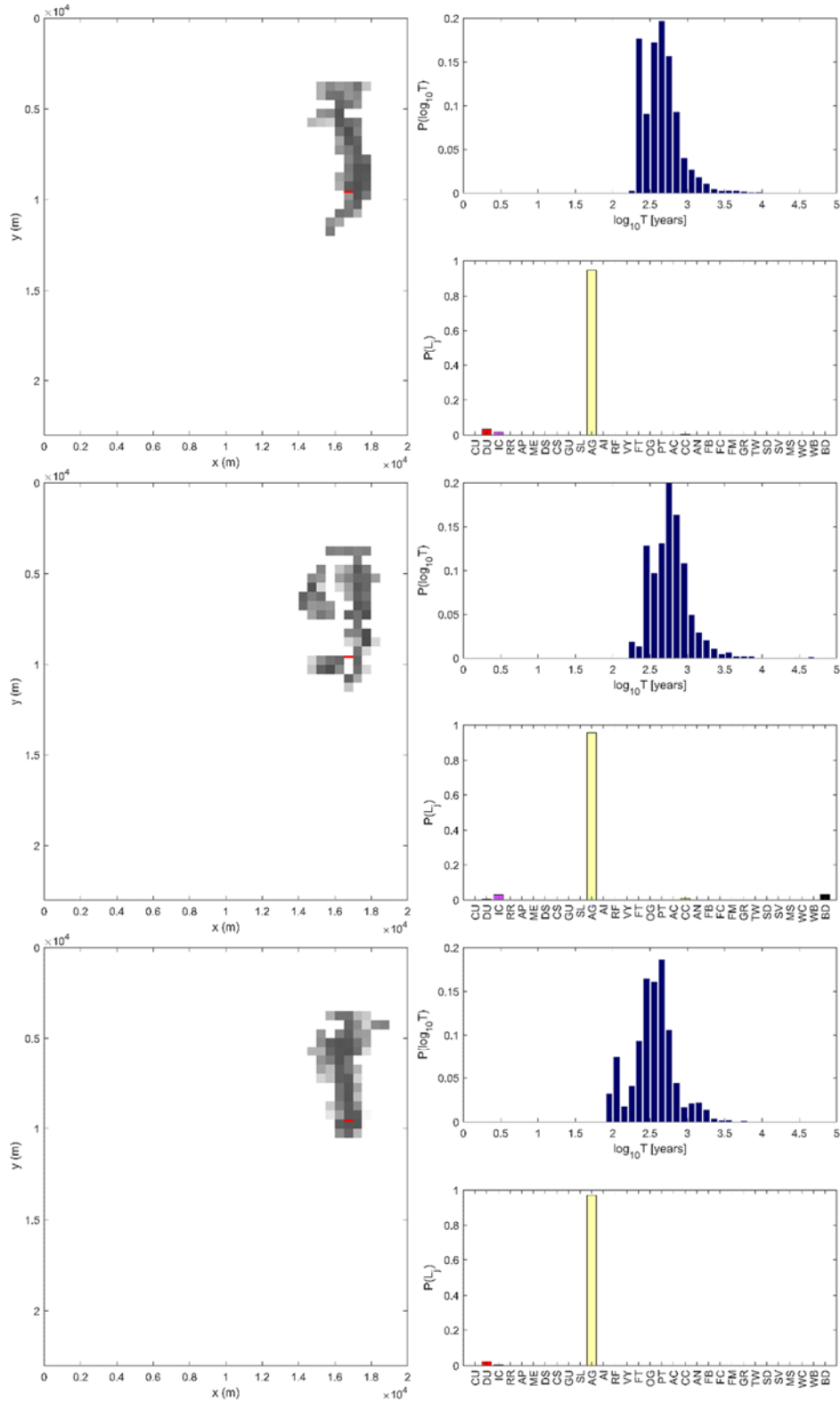


Figure A.1c: Transport results corresponding to Bologna Well 1, realizations 6-8 (top to bottom). In the grayscale map on the left, each cell is colored according to the value of  $\log_{10} F$ , being  $F$  the fraction of the  $N$  particles that are traced back up to the considered cell (white is  $\leq -4$ , black is 0). Pumping Well in red. On the upper-right, histogram of the log-residence time (eq. 2.7). On the bottom-right, land use distribution (eq. 2.6; see Figure 2.2).

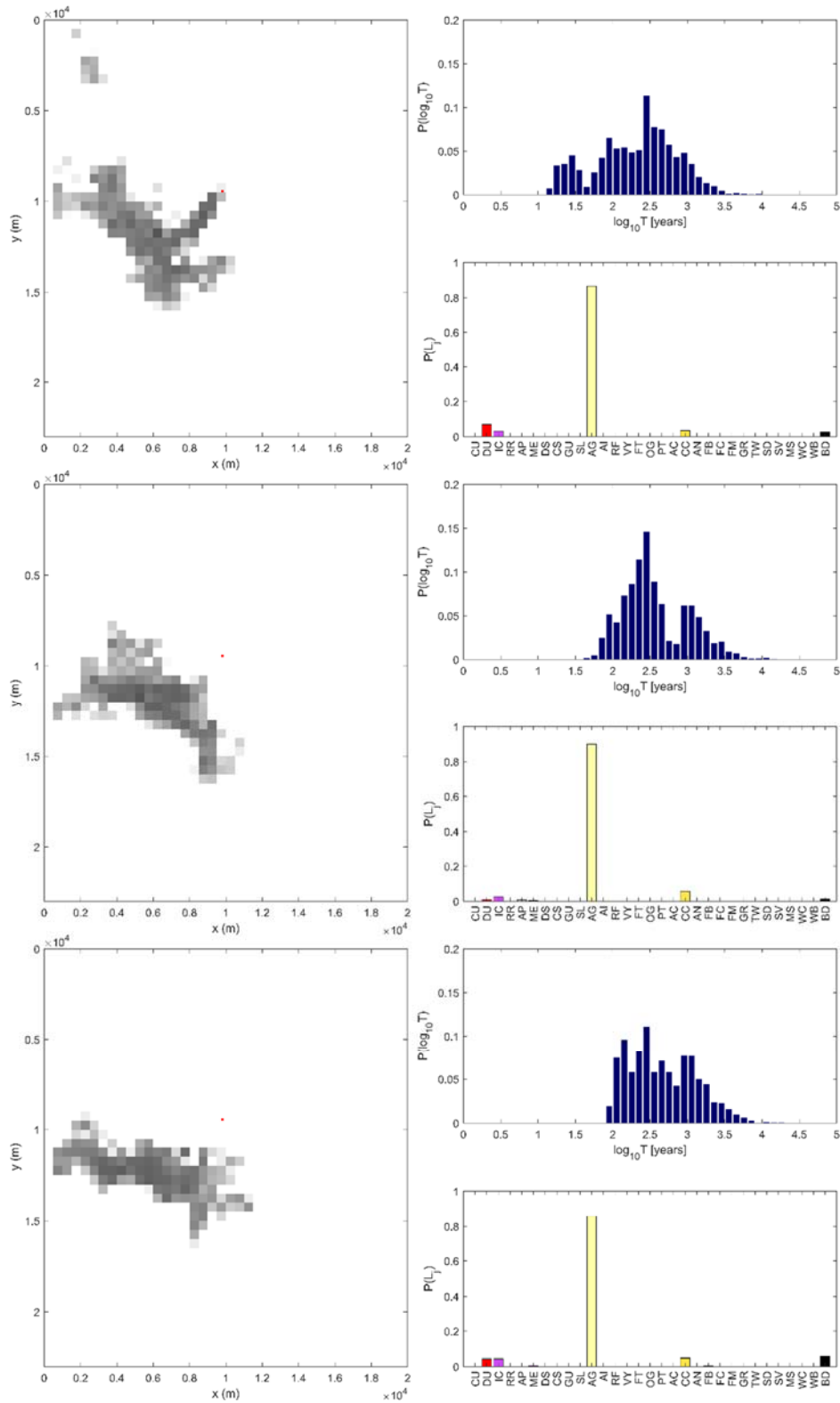


Figure A.2a: Transport results corresponding to Bologna Well 2, realizations 0-2 (top to bottom). In the grayscale map on the left, each cell is colored according to the value of  $\log_{10} F$ , being  $F$  the fraction of the  $N$  particles that are traced back up to the considered cell (white is  $\leq -4$ , black is 0). Pumping Well in red. On the upper-right, histogram of the log-residence time (eq. 2.7). On the bottom-right, land use distribution (eq. 2.6; see Figure 2.2).

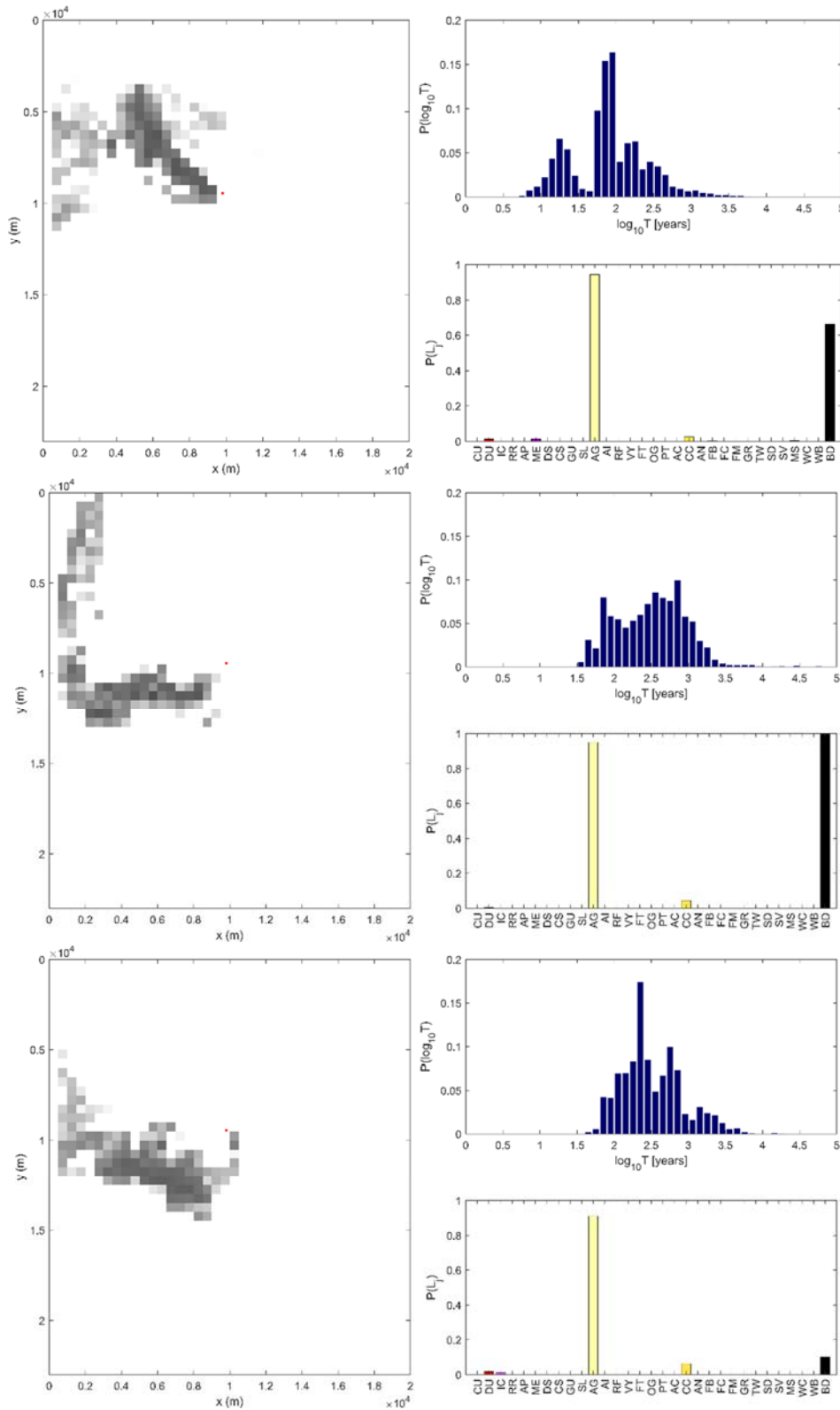


Figure A.2b: Transport results corresponding to Bologna Well 2, realizations 3-5 (top to bottom). In the grayscale map on the left, each cell is colored according to the value of  $\log_{10} F$ , being  $F$  the fraction of the  $N$  particles that are traced back up to the considered cell (white is  $\leq -4$ , black is 0). Pumping Well in red. On the upper-right, histogram of the log-residence time (eq. 2.7). On the bottom-right, land use distribution (eq. 2.6; see Figure 2.2).

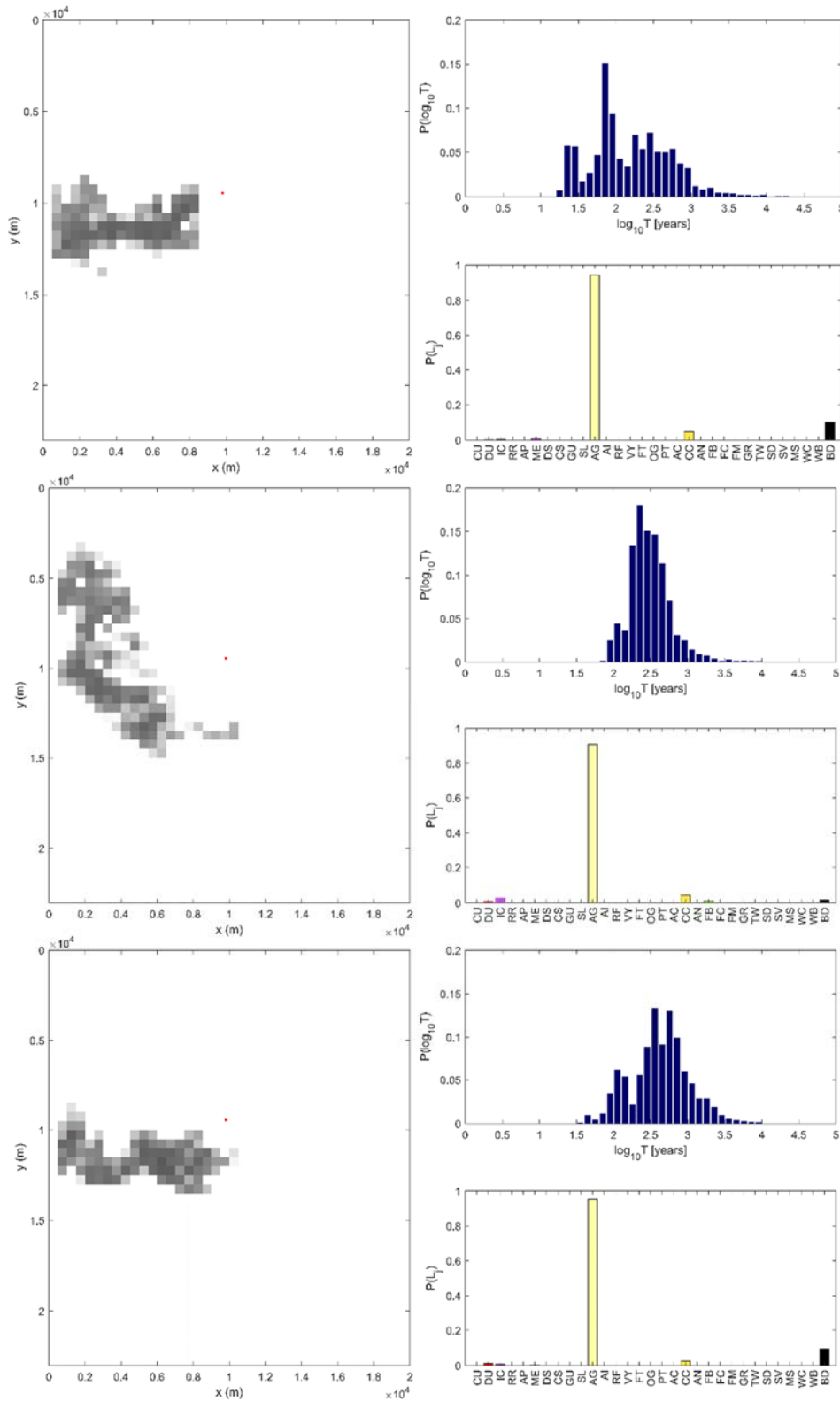


Figure A.2c: Transport results corresponding to Bologna Well 2, realizations 6-8 (top to bottom). In the grayscale map on the left, each cell is colored according to the value of  $\log_{10} F$ , being  $F$  the fraction of the  $N$  particles that are traced back up to the considered cell (white is  $\leq -4$ , black is 0). Pumping Well in red. On the upper-right, histogram of the log-residence time (eq. 2.7). On the bottom-right, land use distribution (eq. 2.6; see Figure 2.2).

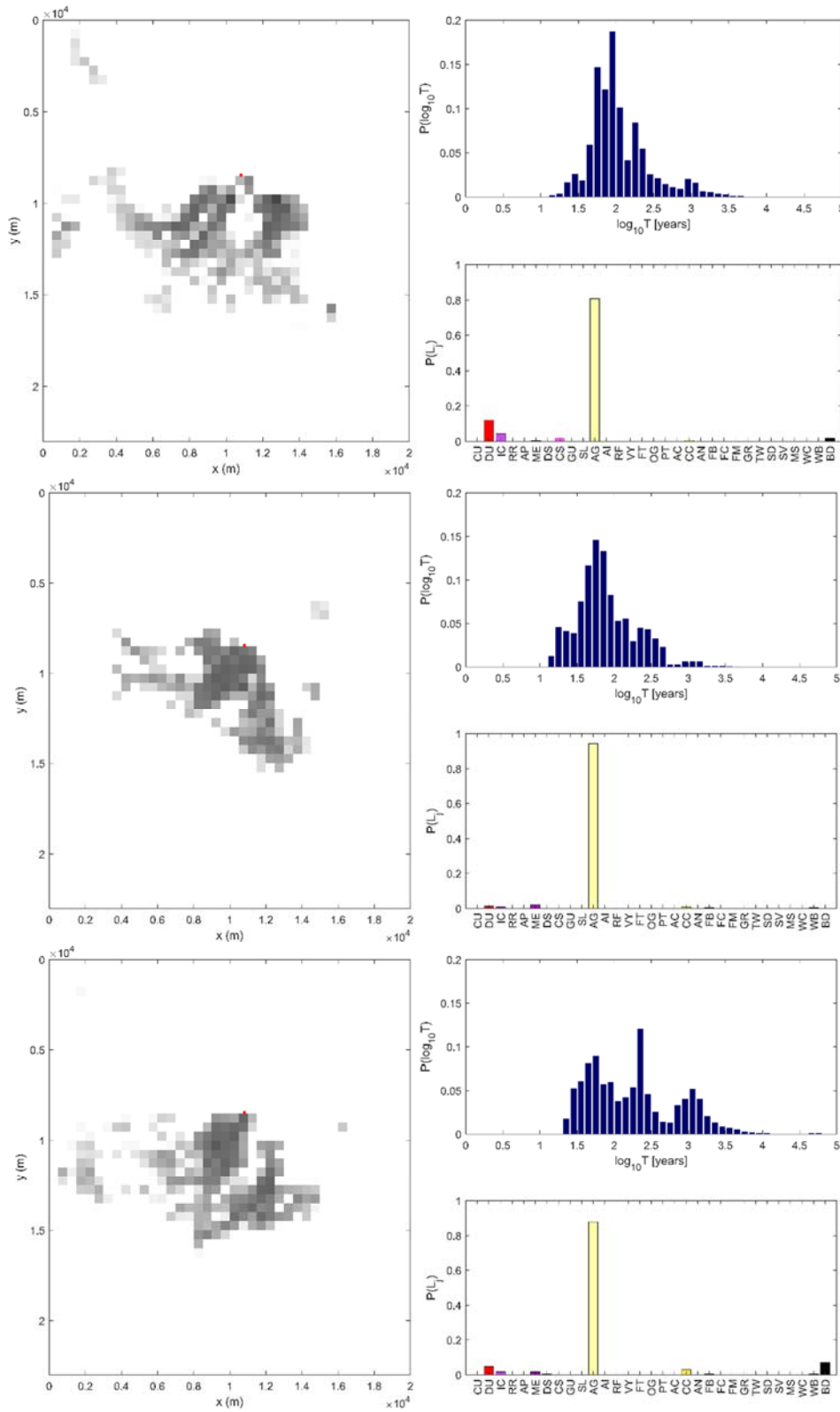


Figure A.3a: Transport results corresponding to Bologna Well 3, realizations 0-2 (top to bottom). In the grayscale map on the left, each cell is colored according to the value of  $\log_{10} F$ , being  $F$  the fraction of the  $N$  particles that are traced back up to the considered cell (white is  $\leq -4$ , black is 0). Pumping Well in red. On the upper-right, histogram of the log-residence time (eq. 2.7). On the bottom-right, land use distribution (eq. 2.6; see Figure 2.2).



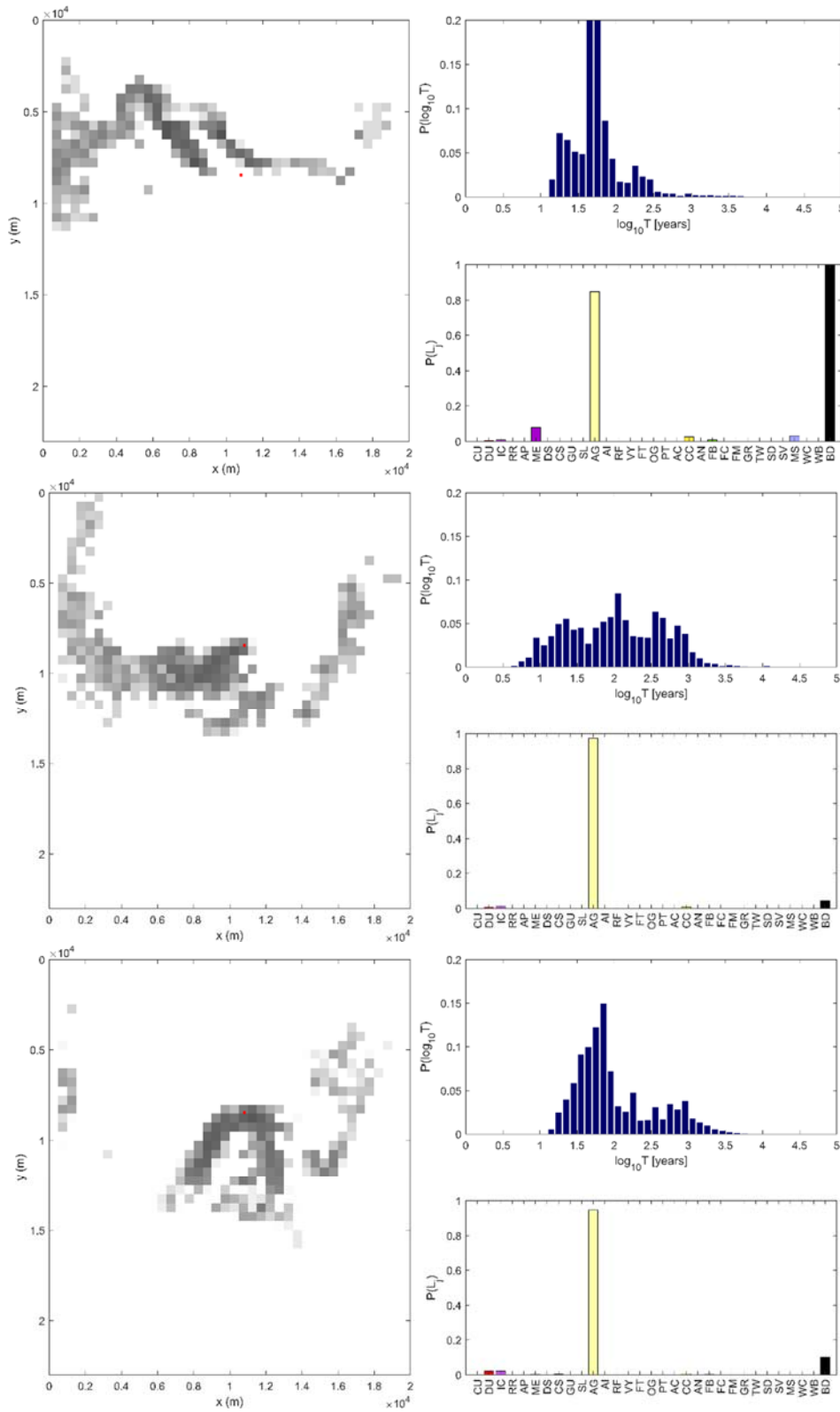


Figure A.3b: Transport results corresponding to Bologna Well 3, realizations 3-5 (top to bottom). In the grayscale map on the left, each cell is colored according to the value of  $\log_{10} F$ , being  $F$  the fraction of the  $N$  particles that are traced back up to the considered cell (white is  $\leq -4$ , black is 0). Pumping Well in red. On the upper-right, histogram of the log-residence time (eq. 2.7). On the bottom-right, land use distribution (eq. 2.6; see Figure 2.2).

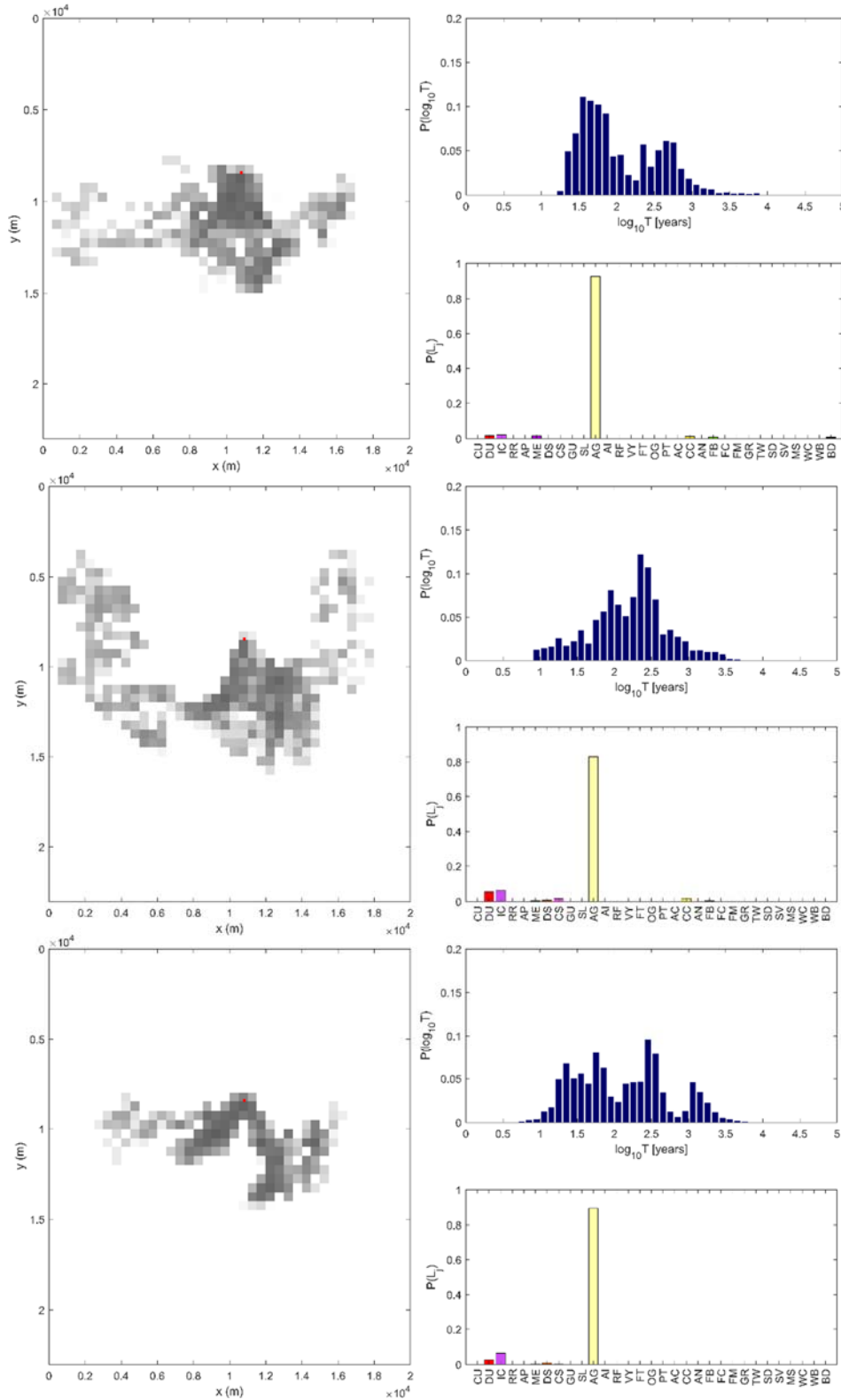


Figure A.3c: Transport results corresponding to Bologna Well 3, realizations 6-8 (top to bottom). In the grayscale map on the left, each cell is colored according to the value of  $\log_{10} F$ , being  $F$  the fraction of the  $N$  particles that are traced back up to the considered cell (white is  $\leq -4$ , black is 0). Pumping Well in red. On the upper-right, histogram of the log-residence time (eq. 2.7). On the bottom-right, land use distribution (eq. 2.6; see Figure 2.2).

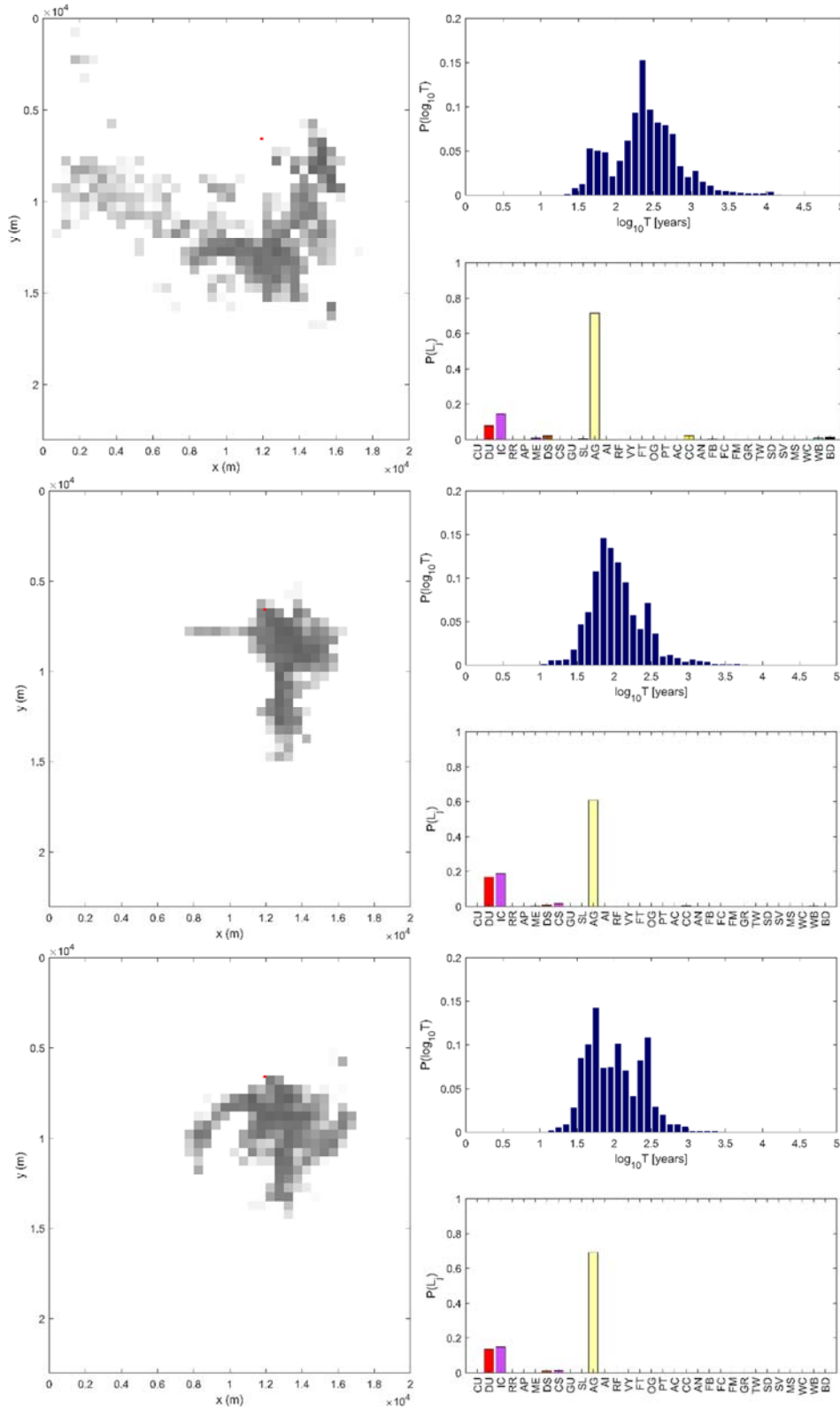


Figure A.4a: Transport results corresponding to Bologna Well 4, realizations 0-2 (top to bottom). In the grayscale map on the left, each cell is colored according to the value of  $\log_{10} F$ , being  $F$  the fraction of the  $N$  particles that are traced back up to the considered cell (white is  $\leq -4$ , black is 0). Pumping Well in red. On the upper-right, histogram of the log-residence time (eq. 2.7). On the bottom-right, land use distribution (eq. 2.6; see Figure 2.2).

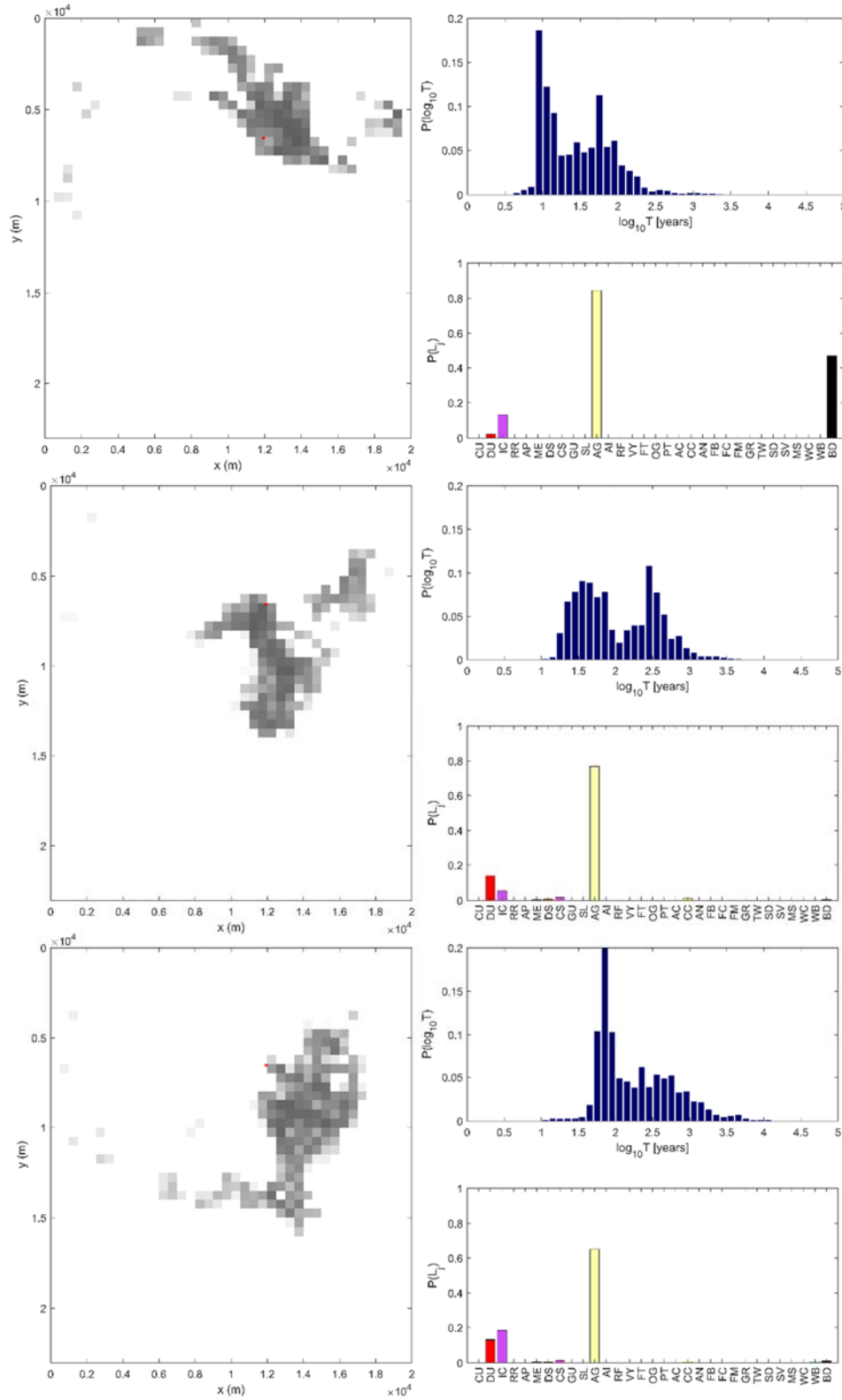


Figure A.4b: Transport results corresponding to Bologna Well 4 realizations 3-5 (top to bottom). In the grayscale map on the left, each cell is colored according to the value of  $\log_{10} F$ , being  $F$  the fraction of the  $N$  particles that are traced back up to the considered cell (white is  $\leq -4$ , black is 0). Pumping Well in red. On the upper-right, histogram of the log-residence time (eq. 2.7). On the bottom-right, land use distribution (eq. 2.6; see Figure 2.2).

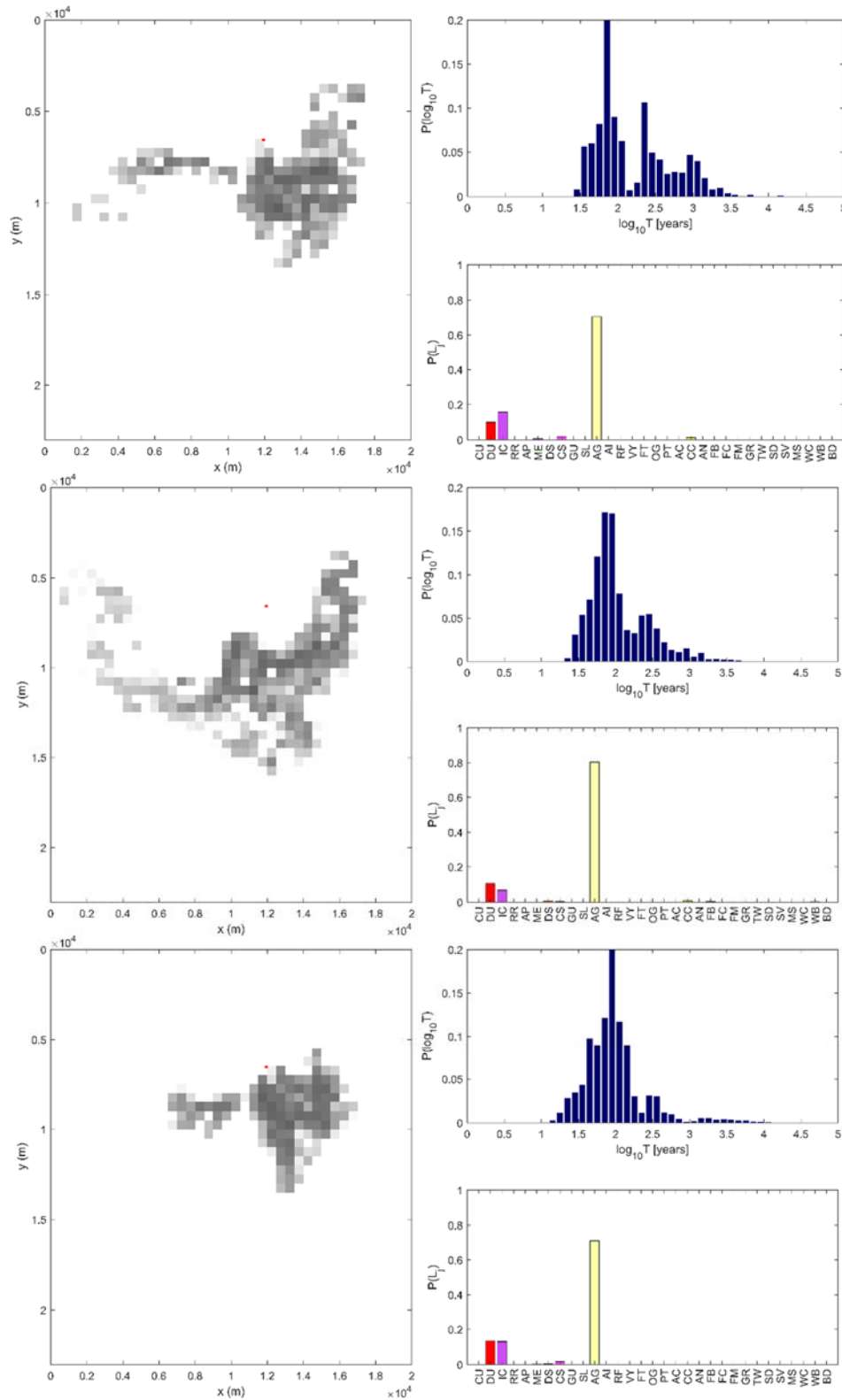


Figure A.4c: Transport results corresponding to Bologna Well 4 realizations 6-8 (top to bottom). In the grayscale map on the left, each cell is colored according to the value of  $\log_{10} F$ , being  $F$  the fraction of the  $N$  particles that are traced back up to the considered cell (white is  $\leq -4$ , black is 0). Pumping Well in red. On the upper-right, histogram of the log-residence time (eq. 2.7). On the bottom-right, land use distribution (eq. 2.6; see Figure 2.2).

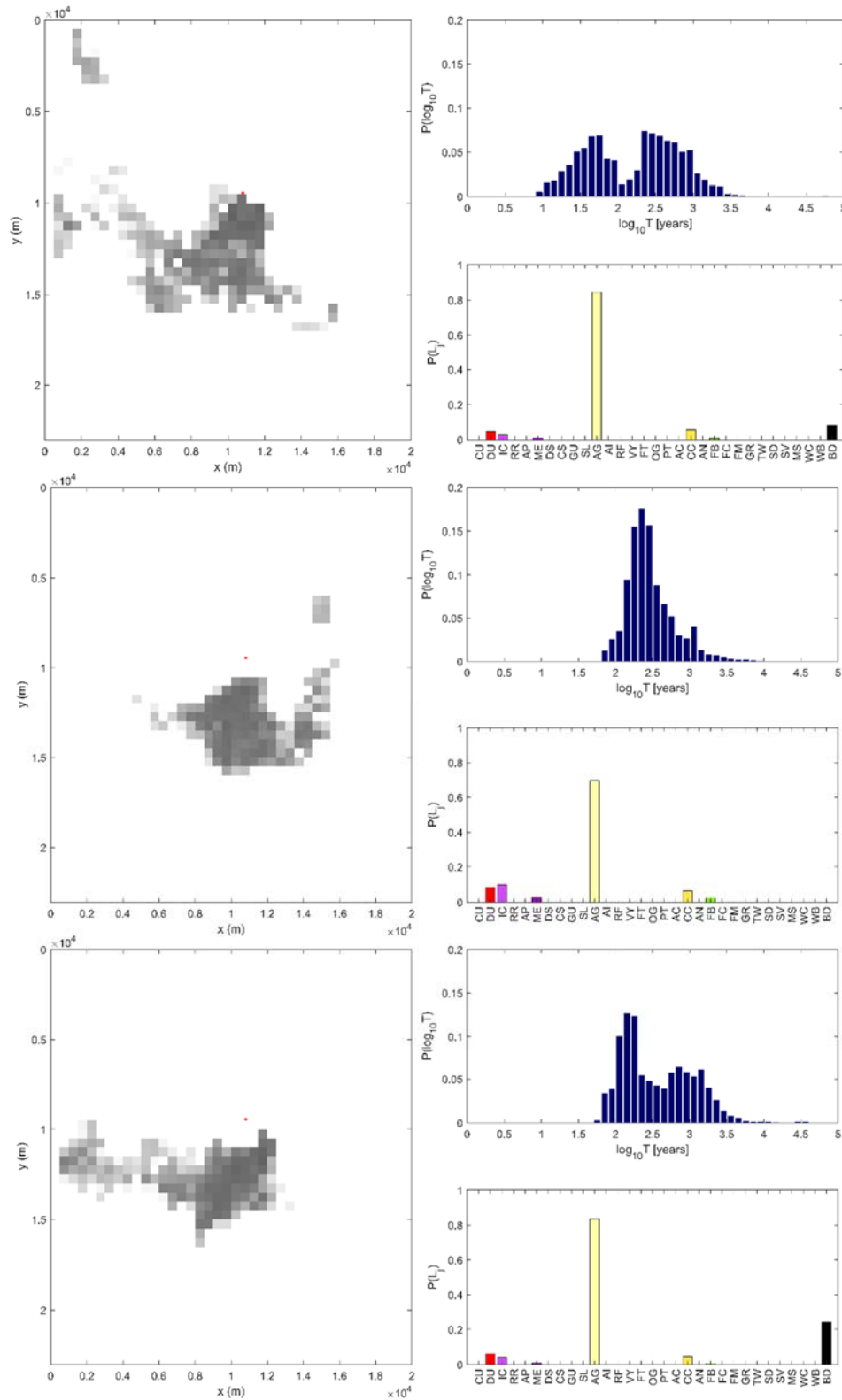


Figure A.5a: Transport results corresponding to Bologna Well 5, realizations 0-2 (top to bottom). In the grayscale map on the left, each cell is colored according to the value of  $\log_{10} F$ , being  $F$  the fraction of the  $N$  particles that are traced back up to the considered cell (white is  $\leq -4$ , black is 0). Pumping Well in red. On the upper-right, histogram of the log-residence time (eq. 2.7). On the bottom-right, land use distribution (eq. 2.6; see Figure 2.2).

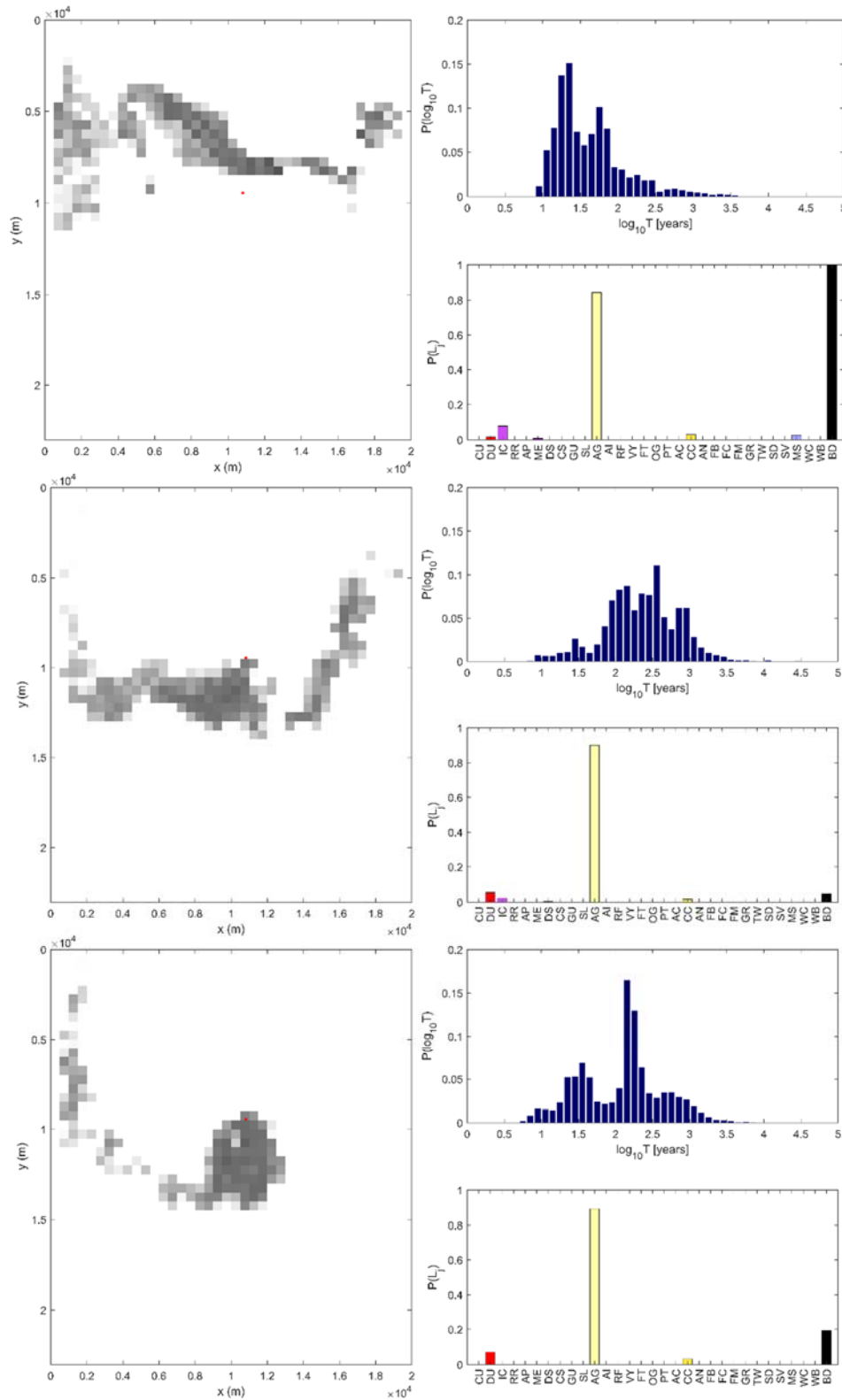


Figure A.5b: Transport results corresponding to Bologna Well 5, realizations 3-5 (top to bottom). In the grayscale map on the left, each cell is colored according to the value of  $\log_{10} F$ , being  $F$  the fraction of the  $N$  particles that are traced back up to the considered cell (white is  $\leq -4$ , black is 0). Pumping Well in red. On the upper-right, histogram of the log-residence time (eq. 2.7). On the bottom-right, land use distribution (eq. 2.6; see Figure 2.2).

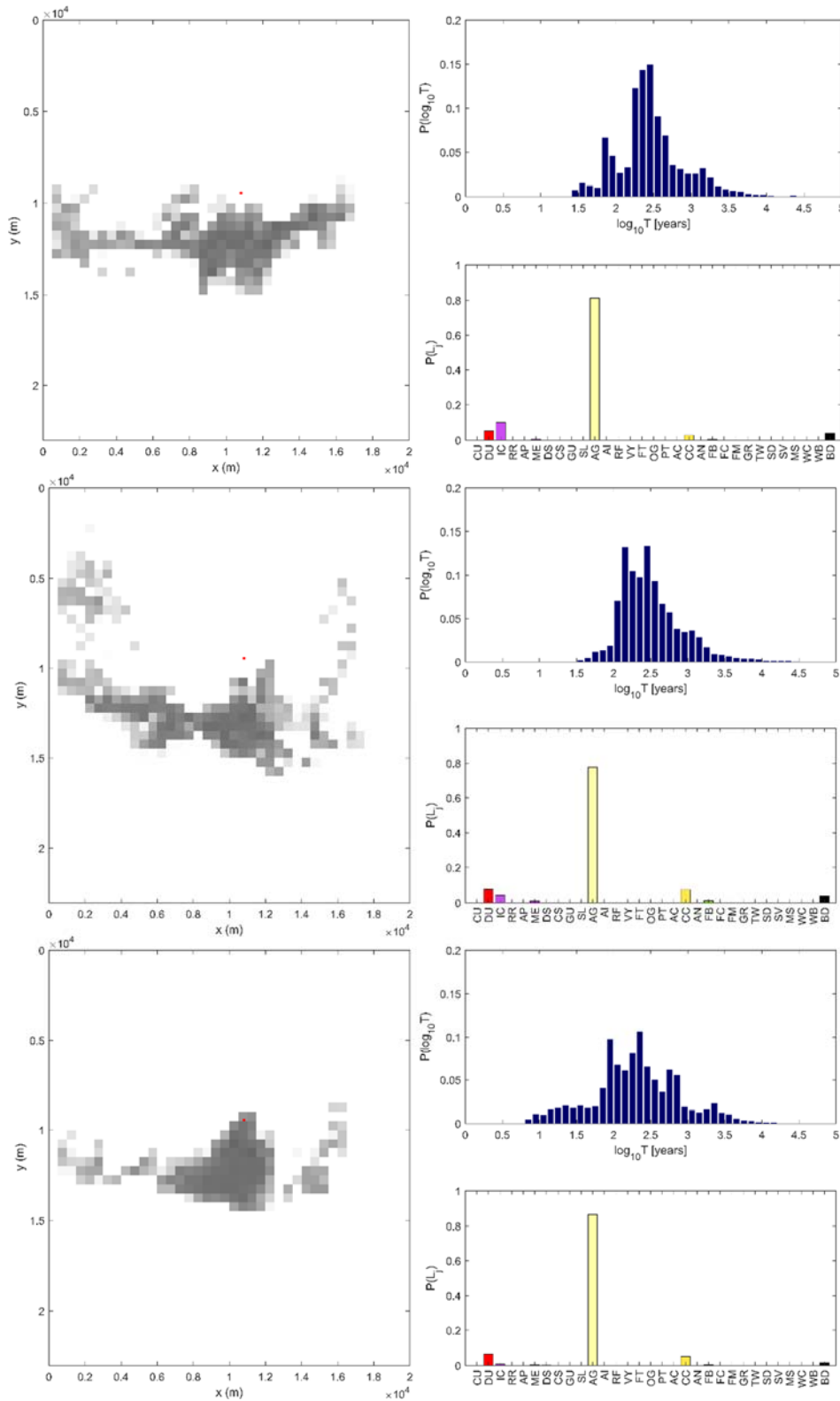


Figure A.5c: Transport results corresponding to Bologna Well 5, realizations 6-8 (top to bottom). In the grayscale map on the left, each cell is colored according to the value of  $\log_{10} F$ , being  $F$  the fraction of the  $N$  particles that are traced back up to the considered cell (white is  $\leq -4$ , black is 0). Pumping Well in red. On the upper-right, histogram of the log-residence time (eq. 2.7). On the bottom-right, land use distribution (eq. 2.6; see Figure 2.2).



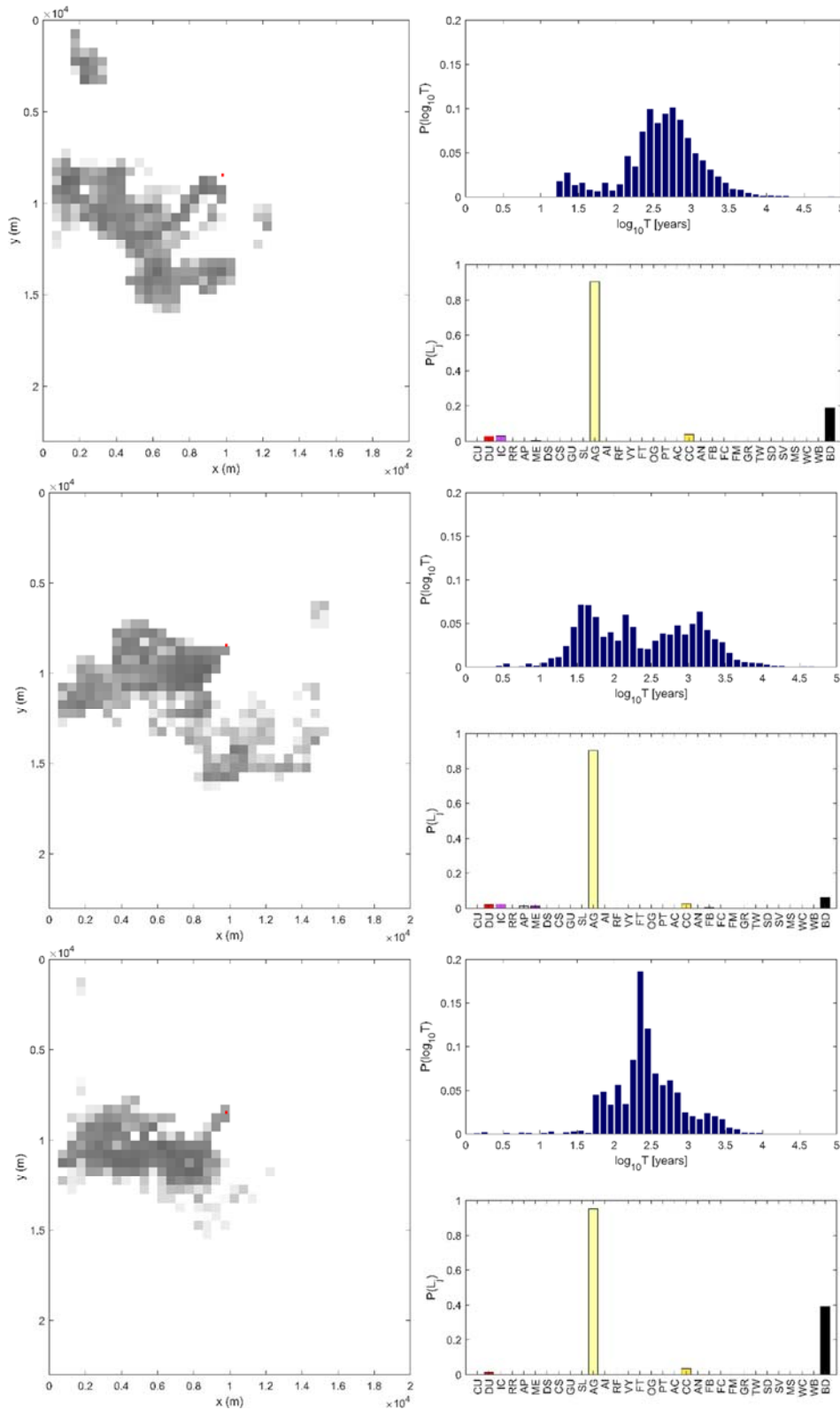


Figure A.6a: Transport results corresponding to Bologna Well 6, realizations 0-2 (top to bottom). In the grayscale map on the left, each cell is colored according to the value of  $\log_{10} F$ , being  $F$  the fraction of the  $N$  particles that are traced back up to the considered cell (white is  $\leq -4$ , black is 0). Pumping Well in red. On the upper-right, histogram of the log-residence time (eq. 2.7). On the bottom-right, land use distribution (eq. 2.6; see Figure 2.2).

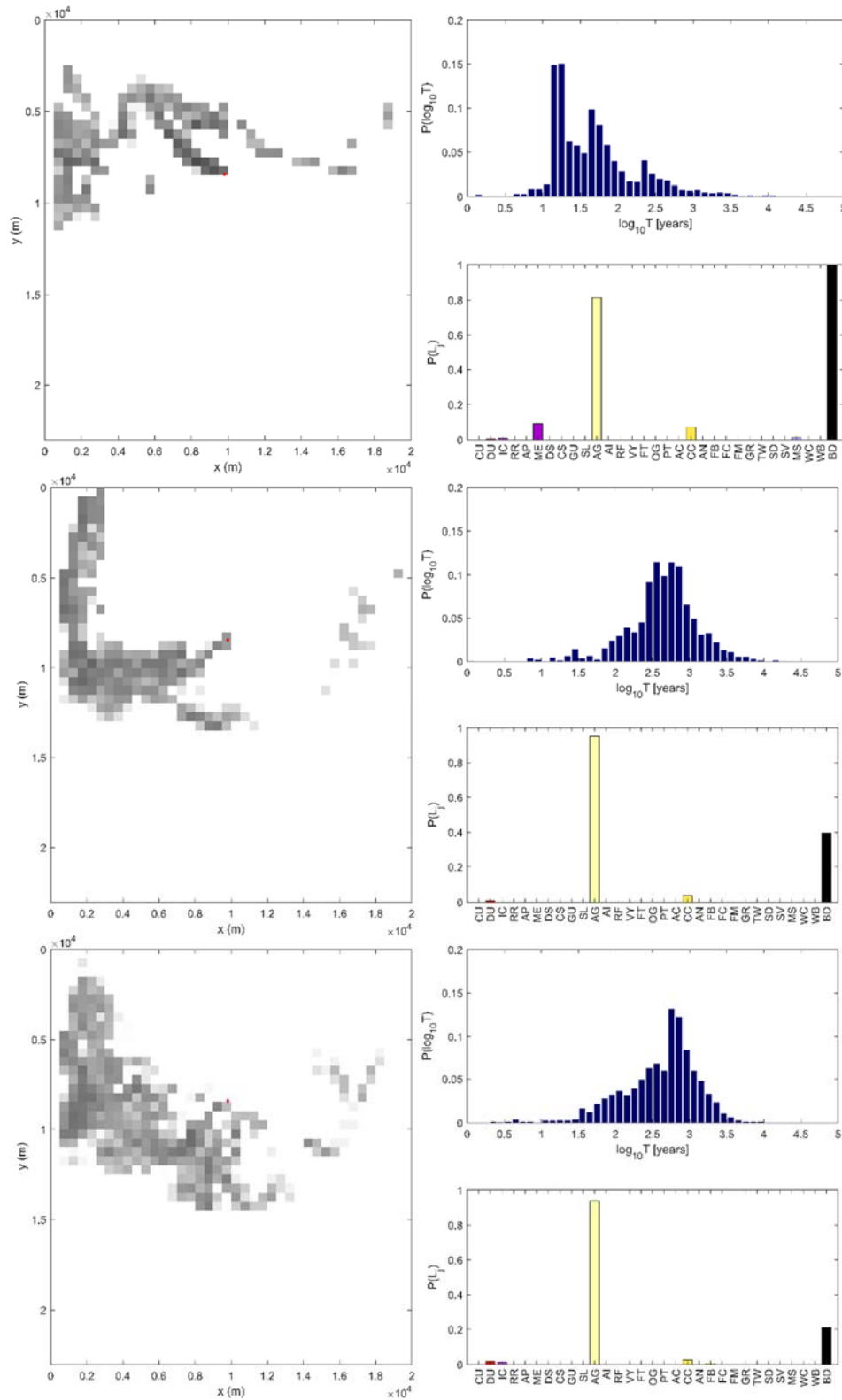


Figure A.6b: Transport results corresponding to Bologna Well 6, realizations 3-5 (top to bottom). In the grayscale map on the left, each cell is colored according to the value of  $\log_{10} F$ , being  $F$  the fraction of the  $N$  particles that are traced back up to the considered cell (white is  $\leq -4$ , black is 0). Pumping Well in red. On the upper-right, histogram of the log-residence time (eq. 2.7). On the bottom-right, land use distribution (eq. 2.6; see Figure 2.2).

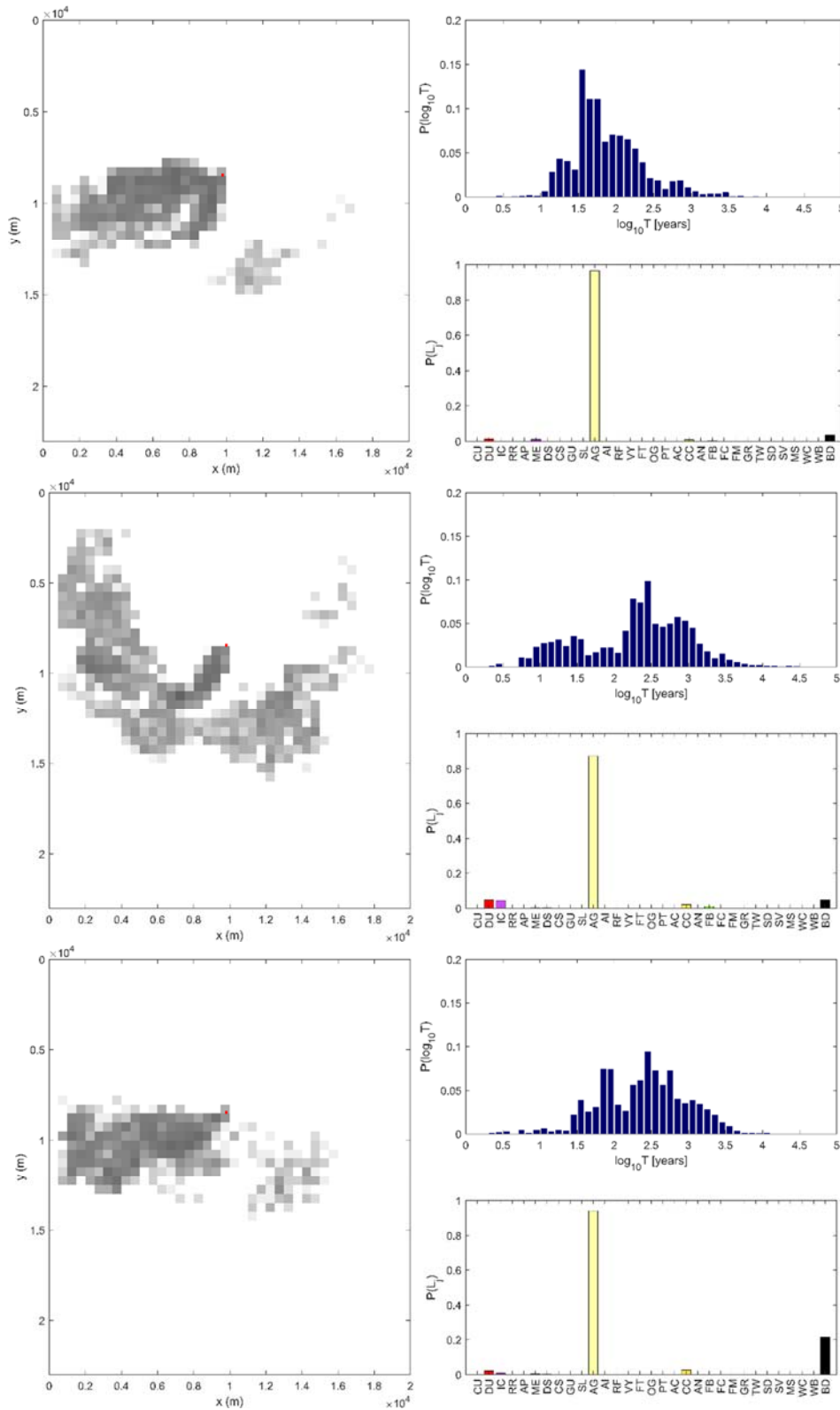


Figure A.6c: Transport results corresponding to Bologna Well 6, realizations 6-8 (top to bottom). In the grayscale map on the left, each cell is colored according to the value of  $\log_{10} F$ , being  $F$  the fraction of the  $N$  particles that are traced back up to the considered cell (white is  $\leq -4$ , black is 0). Pumping Well in red. On the upper-right, histogram of the log-residence time (eq. 2.7). On the bottom-right, land use distribution (eq. 2.6; see Figure 2.2).

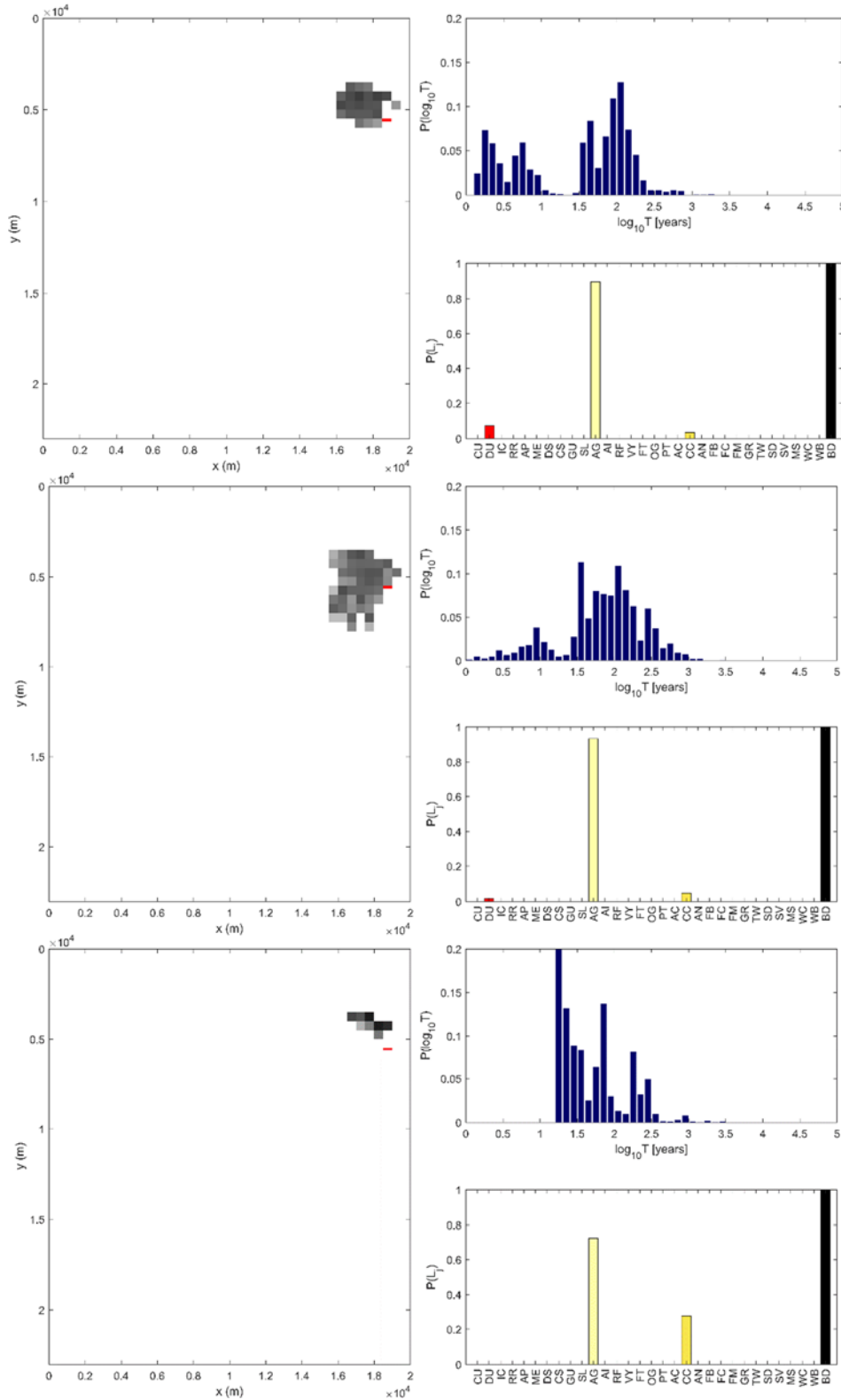


Figure A.7a: Transport results corresponding to Bologna Well 7 realizations 0-2 (top to bottom). In the grayscale map on the left, each cell is colored according to the value of  $\log_{10} F$ , being  $F$  the fraction of the  $N$  particles that are traced back up to the considered cell (white is  $\leq -4$ , black is 0). Pumping Well in red. On the upper-right, histogram of the log-residence time (eq. 2.7). On the bottom-right, land use distribution (eq. 2.6; see Figure 2.2).

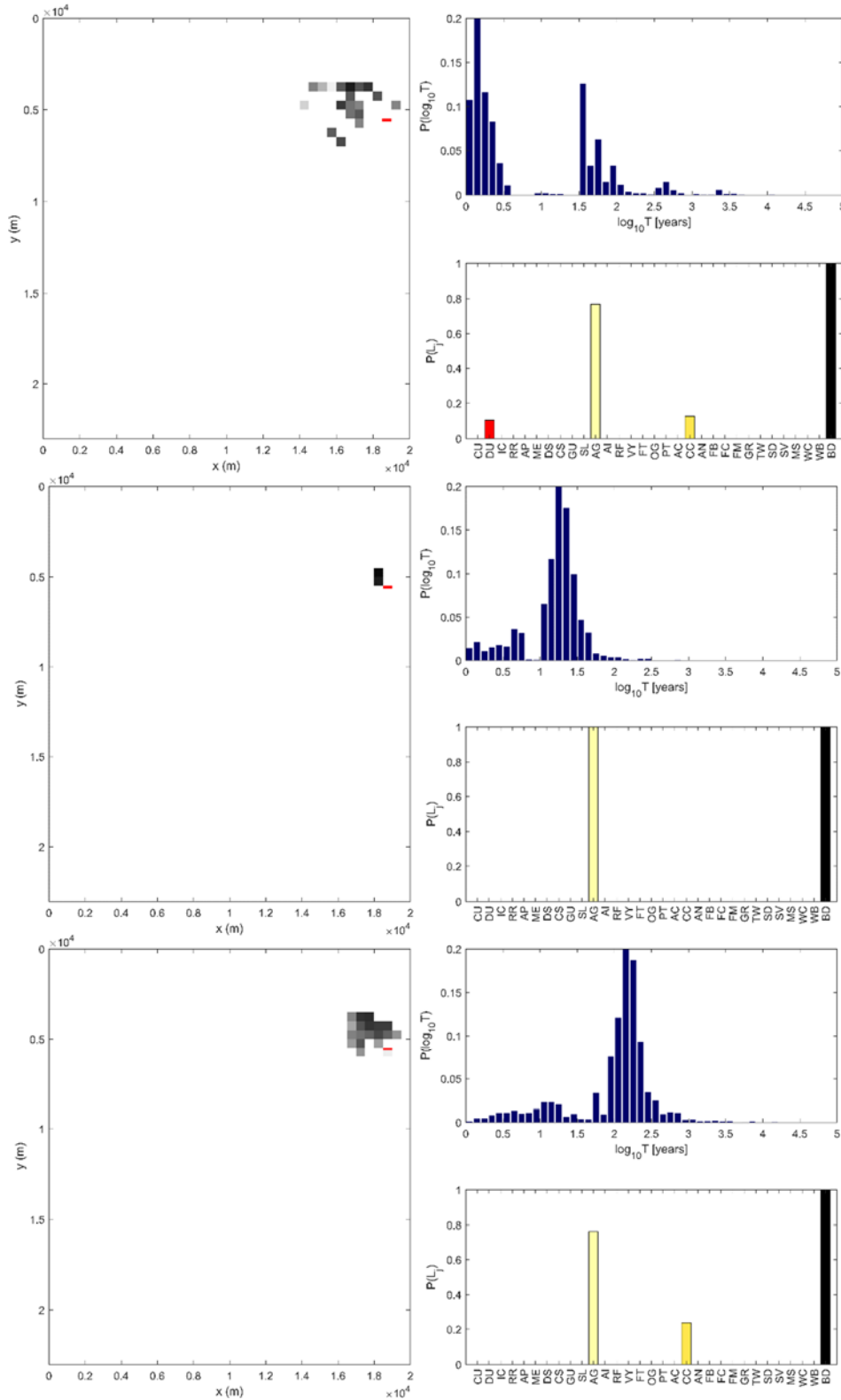


Figure A.7b: Transport results corresponding to Bologna Well 7, realizations 3-5 (top to bottom). In the grayscale map on the left, each cell is colored according to the value of  $\log_{10} F$ , being  $F$  the fraction of the  $N$  particles that are traced back up to the considered cell (white is  $\leq -4$ , black is 0). Pumping Well in red. On the upper-right, histogram of the log-residence time (eq. 2.7). On the bottom-right, land use distribution (eq. 2.6; see Figure 2.2).

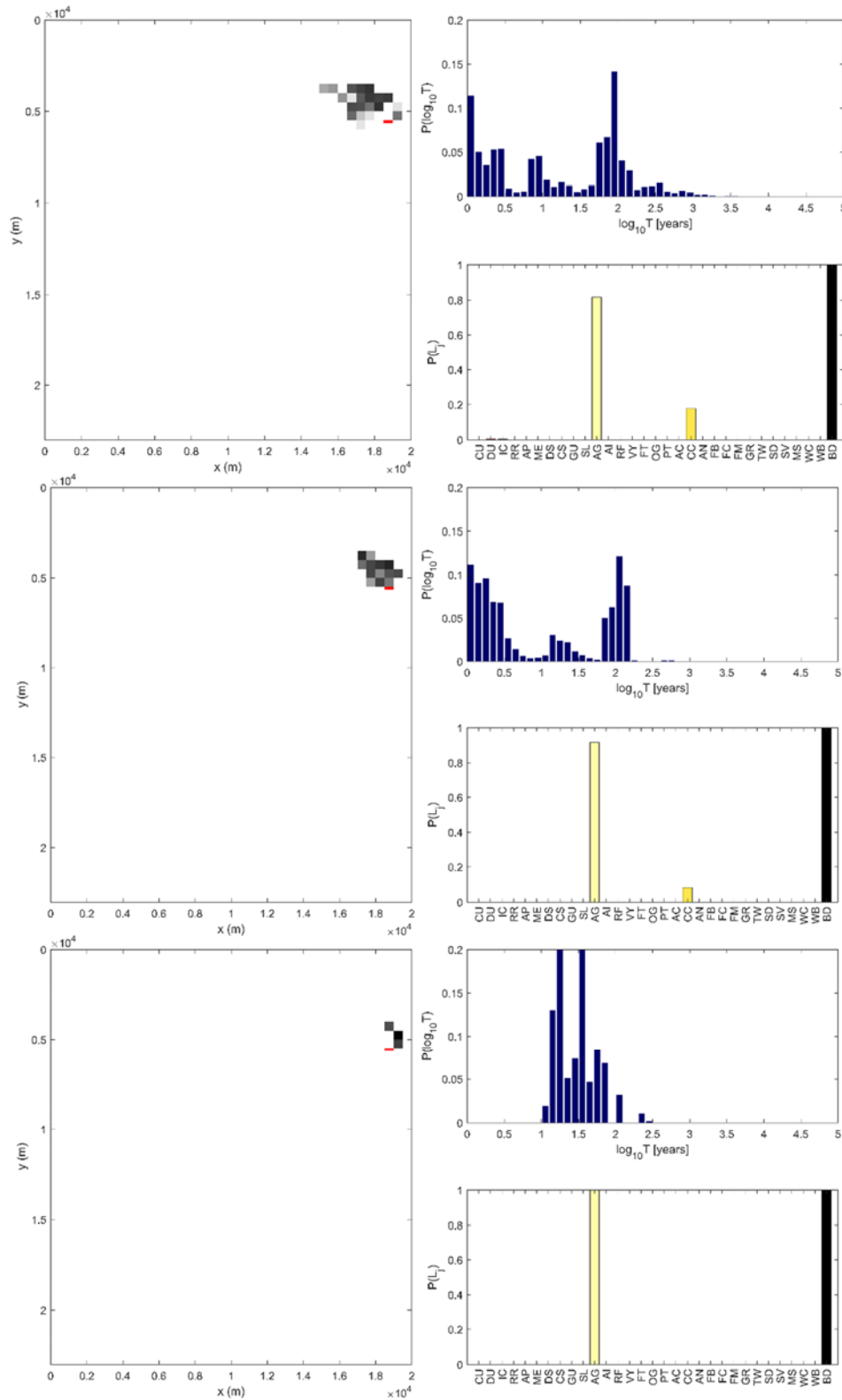


Figure A.7c: Transport results corresponding to Bologna Well 7, realizations 6-8 (top to bottom). In the grayscale map on the left, each cell is colored according to the value of  $\log_{10} F$ , being  $F$  the fraction of the  $N$  particles that are traced back up to the considered cell (white is  $\leq -4$ , black is 0). Pumping Well in red. On the upper-right, histogram of the log-residence time (eq. 2.7). On the bottom-right, land use distribution (eq. 2.6; see Figure 2.2).

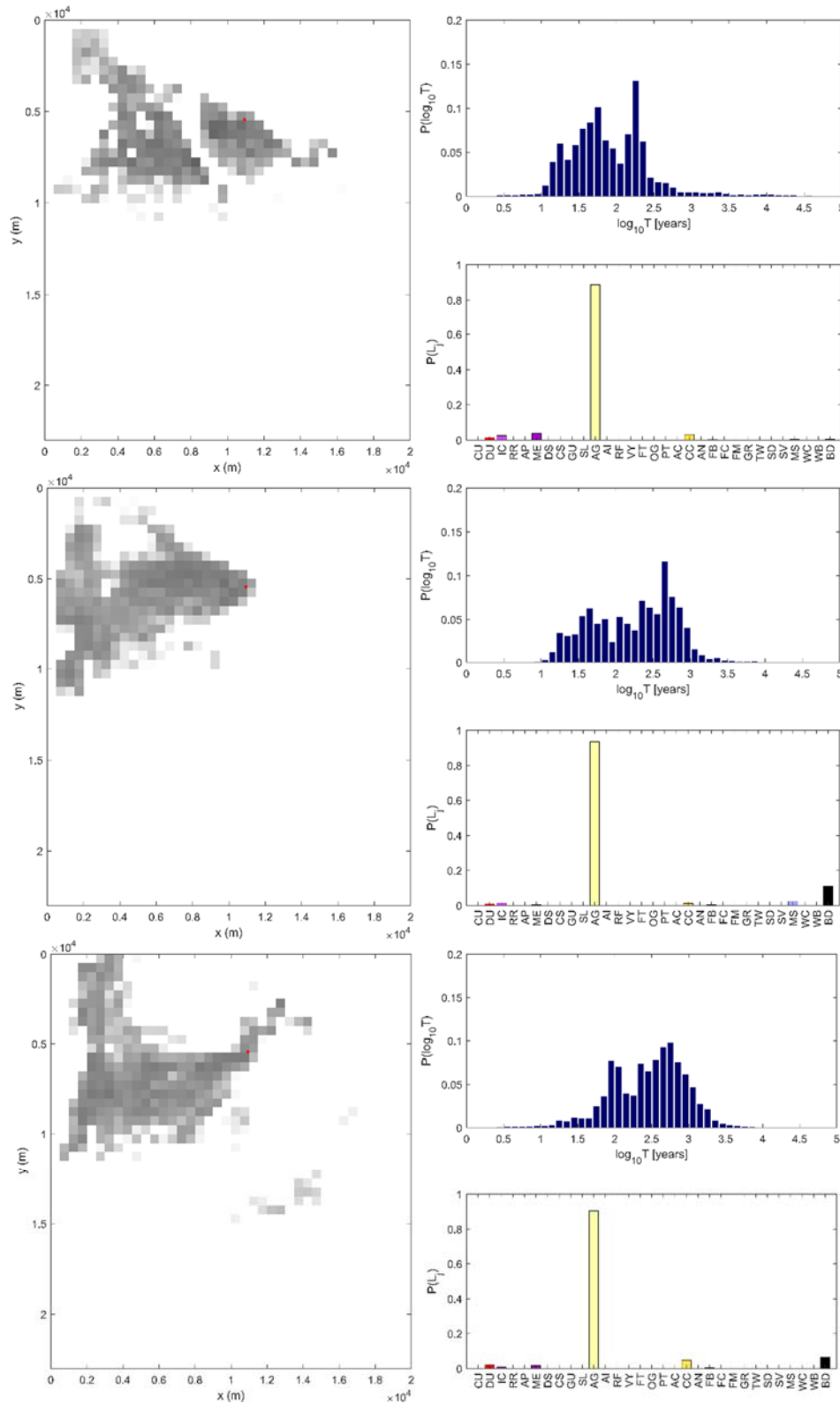


Figure A.8a: Transport results corresponding to Bologna Well 8, realizations 0-2 (top to bottom). In the grayscale map on the left, each cell is colored according to the value of  $\log_{10} F$ , being  $F$  the fraction of the  $N$  particles that are traced back up to the considered cell (white is  $\leq -4$ , black is 0). Pumping Well in red. On the upper-right, histogram of the log-residence time (eq. 2.7). On the bottom-right, land use distribution (eq. 2.6; see Figure 2.2).

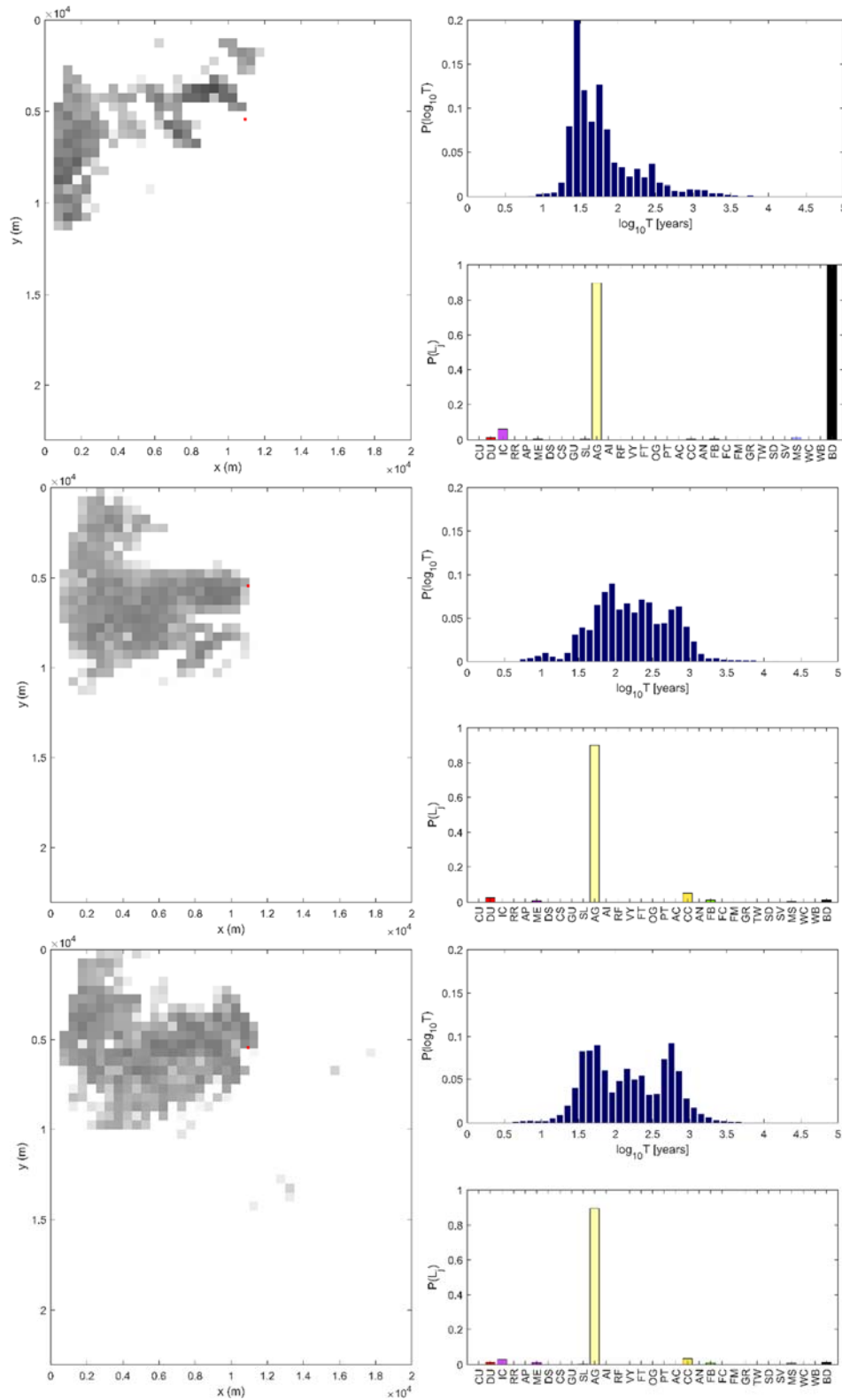


Figure A.8b: Transport results corresponding to Bologna Well 8, realizations 3-5 (top to bottom). In the grayscale map on the left, each cell is colored according to the value of  $\log_{10} F$ , being  $F$  the fraction of the  $N$  particles that are traced back up to the considered cell (white is  $\leq -4$ , black is 0). Pumping Well in red. On the upper-right, histogram of the log-residence time (eq. 2.7). On the bottom-right, land use distribution (eq. 2.6; see Figure 2.2).



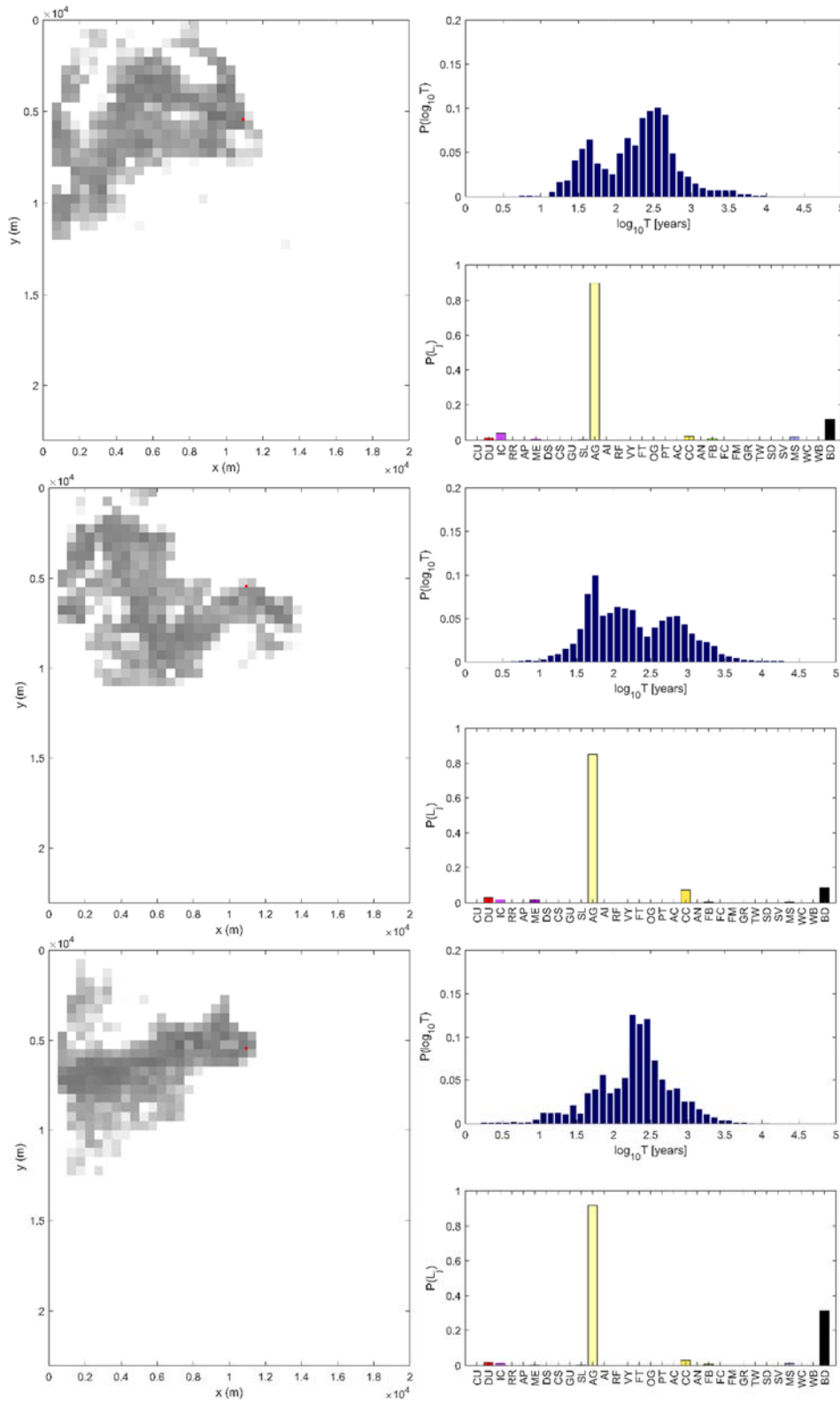


Figure A.8c: Transport results corresponding to Bologna Well 8, realizations 6-8 (top to bottom). In the grayscale map on the left, each cell is colored according to the value of  $\log_{10} F$ , being  $F$  the fraction of the  $N$  particles that are traced back up to the considered cell (white is  $\leq -4$ , black is 0). Pumping Well in red. On the upper-right, histogram of the log-residence time (eq. 2.7). On the bottom-right, land use distribution (eq. 2.6; see Figure 2.2).

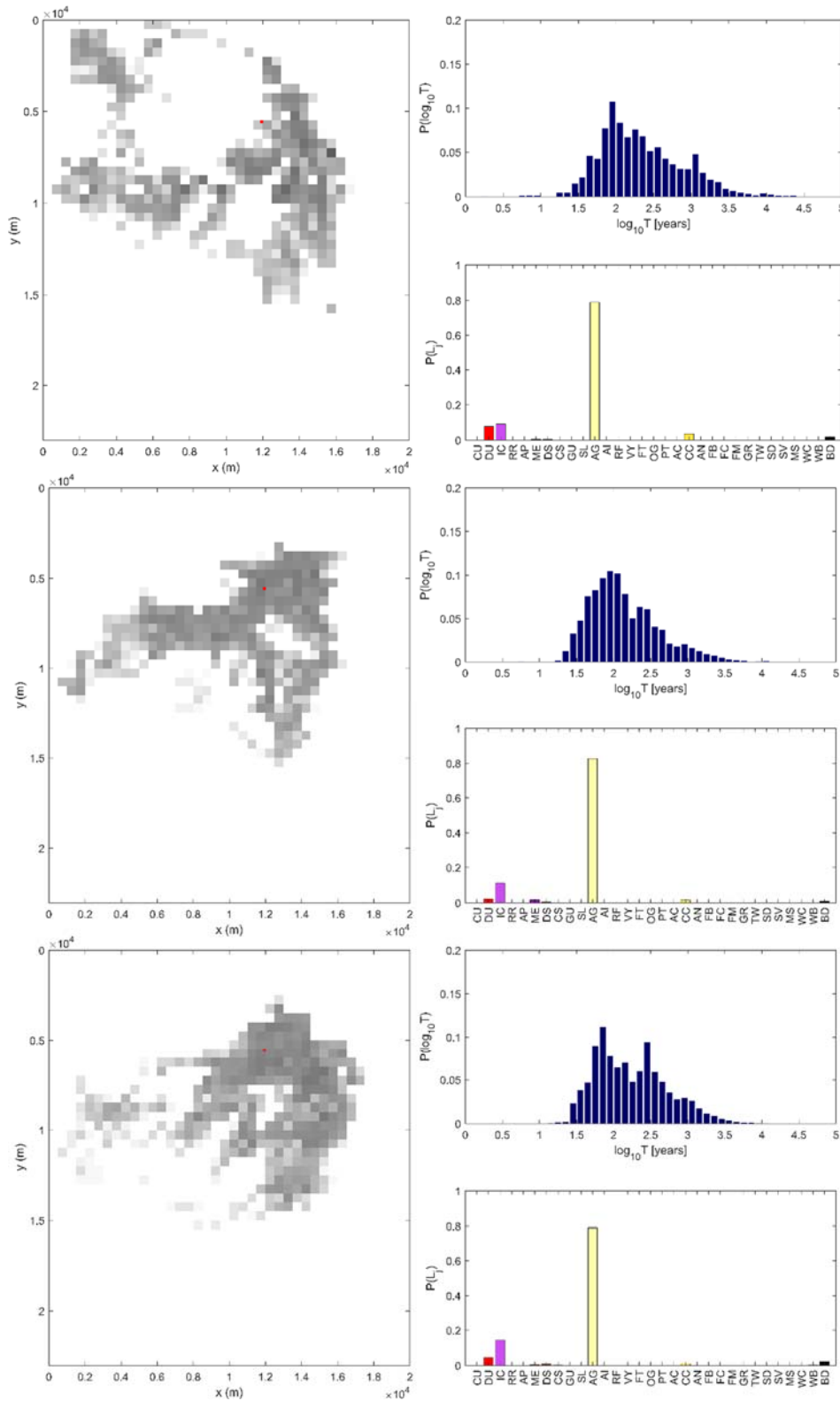


Figure A.9a: Transport results corresponding to Bologna Well 9, realizations 0-2 (top to bottom). In the grayscale map on the left, each cell is colored according to the value of  $\log_{10} F$ , being  $F$  the fraction of the  $N$  particles that are traced back up to the considered cell (white is  $\leq -4$ , black is 0). Pumping Well in red. On the upper-right, histogram of the log-residence time (eq. 2.7). On the bottom-right, land use distribution (eq. 2.6; see Figure 2.2).

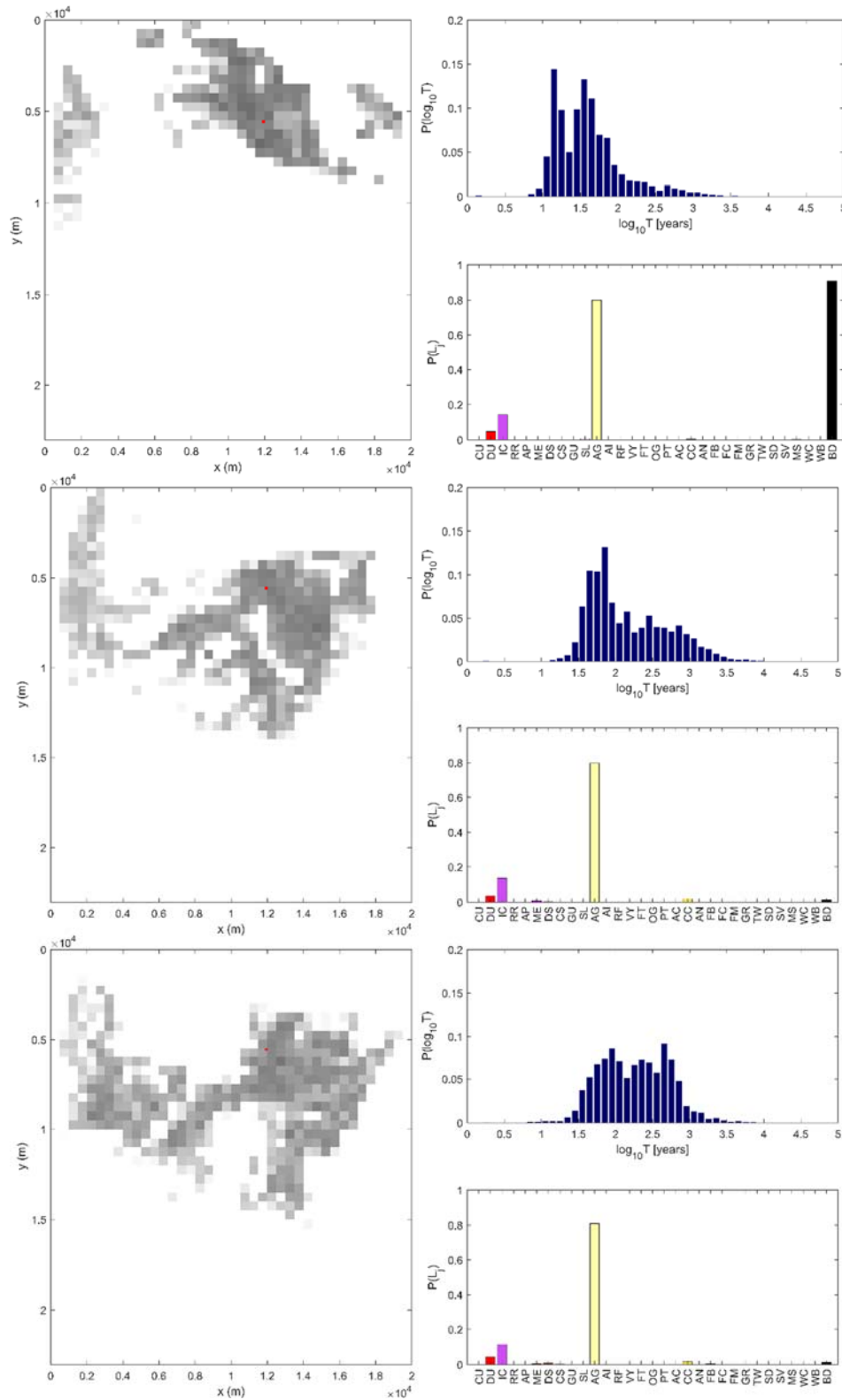


Figure A.9b: Transport results corresponding to Bologna Well 9, realizations 3-5 (top to bottom). In the grayscale map on the left, each cell is colored according to the value of  $\log_{10} F$ , being  $F$  the fraction of the  $N$  particles that are traced back up to the considered cell (white is  $\leq -4$ , black is 0). Pumping Well in red. On the upper-right, histogram of the log-residence time (eq. 2.7). On the bottom-right, land use distribution (eq. 2.6; see Figure 2.2).

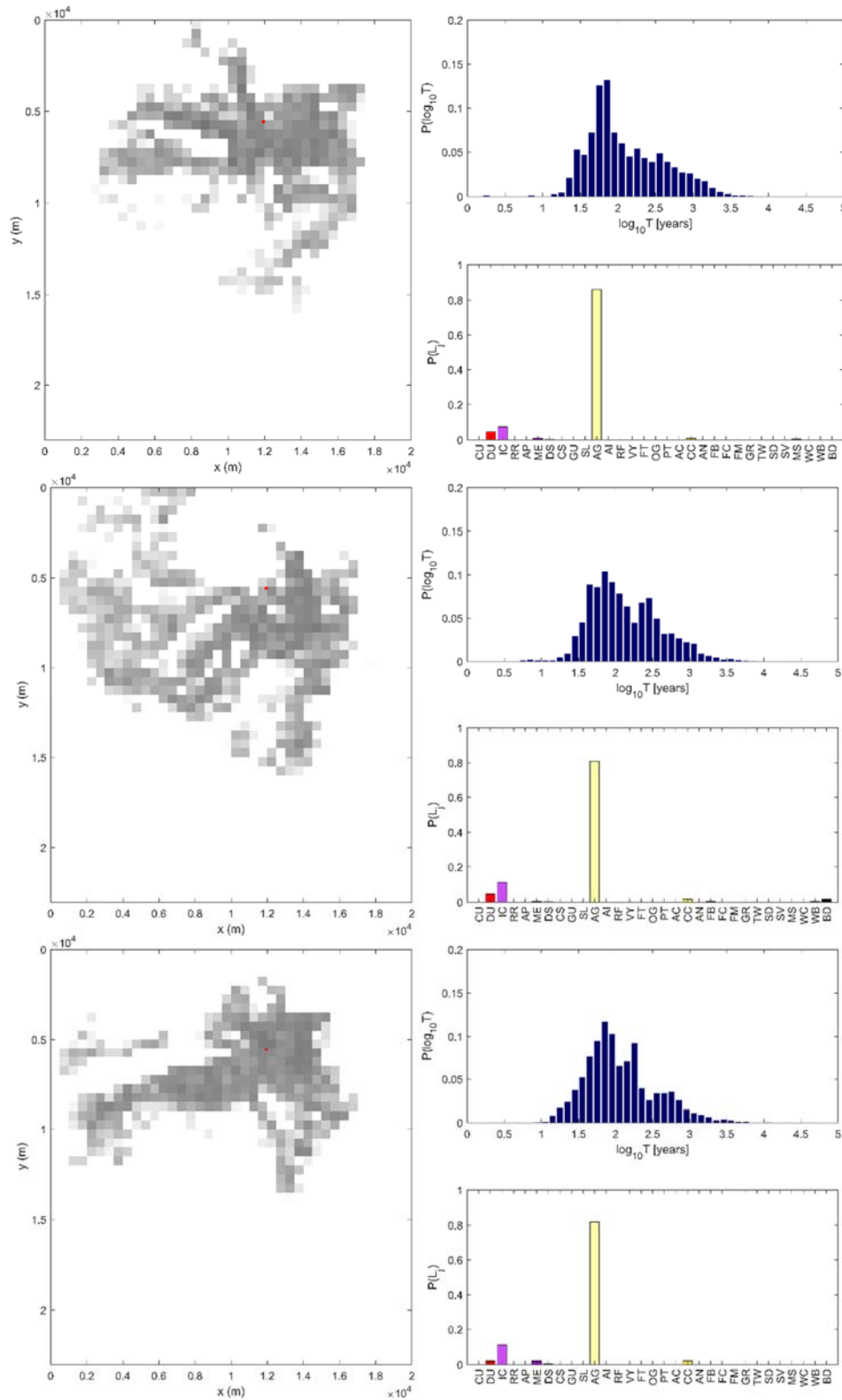


Figure A.9c: Transport results corresponding to Bologna Well 9, realizations 6-8 (top to bottom). In the grayscale map on the left, each cell is colored according to the value of  $\log_{10} F$ , being  $F$  the fraction of the  $N$  particles that are traced back up to the considered cell (white is  $\leq -4$ , black is 0). Pumping Well in red. On the upper-right, histogram of the log-residence time (eq. 2.7). On the bottom-right, land use distribution (eq. 2.6; see Figure 2.2).

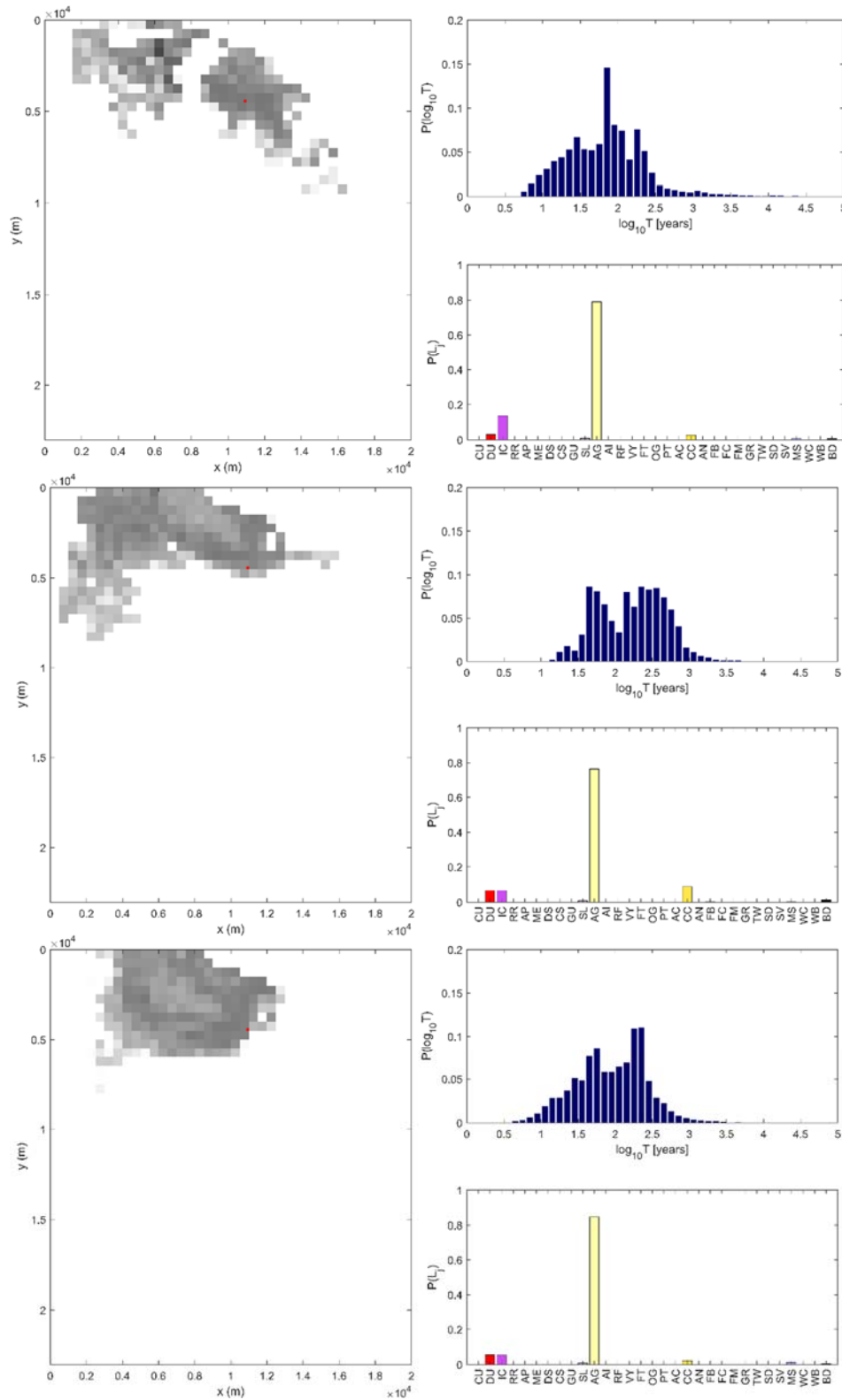


Figure A.10a: Transport results corresponding to Bologna Well 10, realizations 0-2 (top to bottom). In the grayscale map on the left, each cell is colored according to the value of  $\log_{10} F$ , being  $F$  the fraction of the  $N$  particles that are traced back up to the considered cell (white is  $\leq -4$ , black is 0). Pumping Well in red. On the upper-right, histogram of the log-residence time (eq. 2.7). On the bottom-right, land use distribution (eq. 2.6; see Figure 2.2).

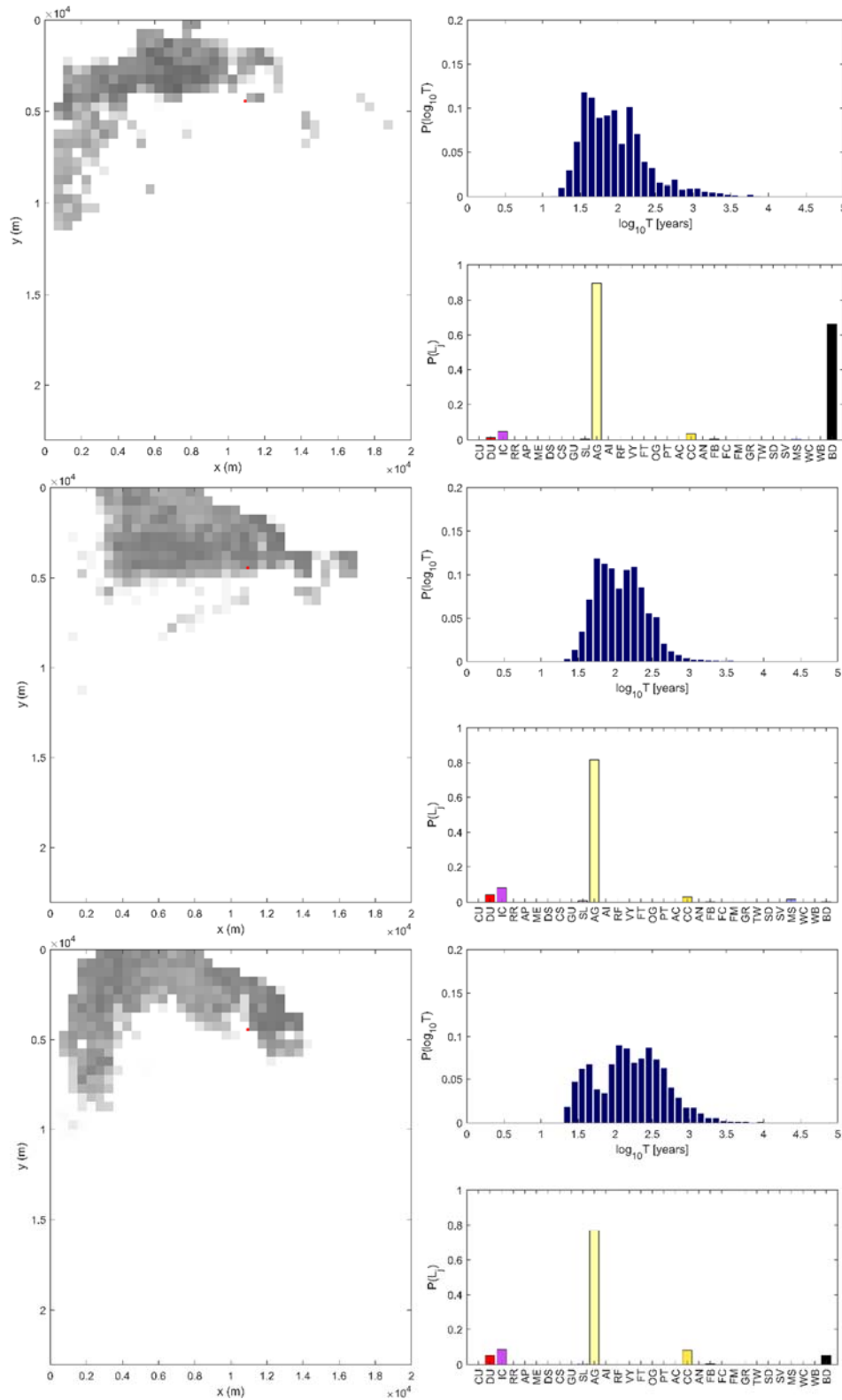


Figure A.10b: Transport results corresponding to Bologna Well 10, realizations 3-5 (top to bottom). In the grayscale map on the left, each cell is colored according to the value of  $\log_{10} F$ , being  $F$  the fraction of the  $N$  particles that are traced back up to the considered cell (white is  $\leq -4$ , black is 0). Pumping Well in red. On the upper-right, histogram of the log-residence time (eq. 2.7). On the bottom-right, land use distribution (eq. 2.6; see Figure 2.2).

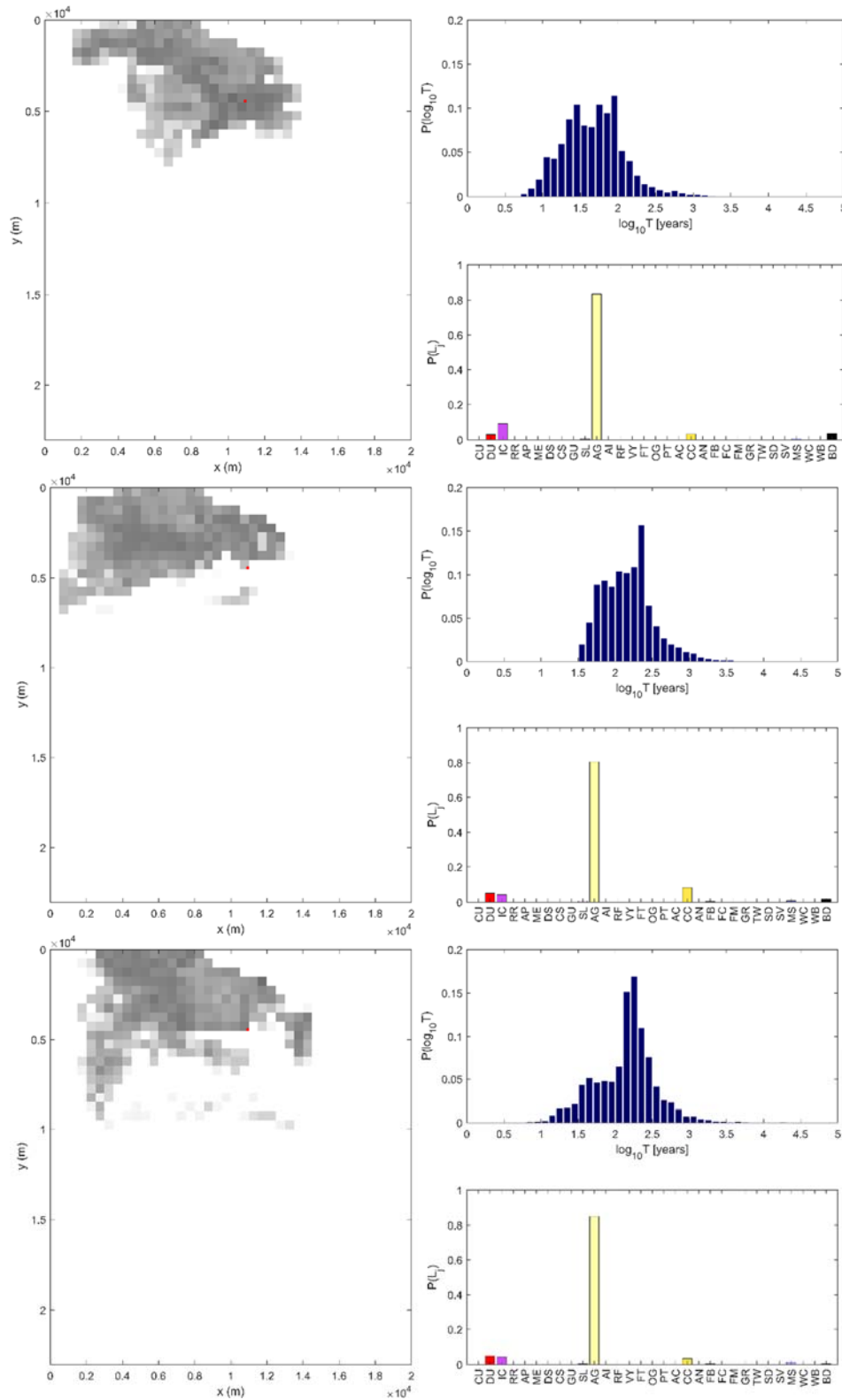


Figure A.10c: Transport results corresponding to Bologna Well 10, realizations 6-8 (top to bottom). In the grayscale map on the left, each cell is colored according to the value of  $\log_{10} F$ , being  $F$  the fraction of the  $N$  particles that are traced back up to the considered cell (white is  $\leq -4$ , black is 0). Pumping Well in red. On the upper-right, histogram of the log-residence time (eq. 2.7). On the bottom-right, land use distribution (eq. 2.6; see Figure 2.2).